Doctoral Dissertation

Study of muon trigger performances
with the ATLAS detector at the LHC

Graduate School of Science and Technology,
Kobe University
Chihiro Omachi

January 2010

Abstract

The LHC (Large Hadron Collider) at CERN laboratory, Geneva, Switzerland, started its operation in 2009. The LHC will achieve high-energy proton-proton collisions with the center-of-mass energy at 14TeV, seven times higher than previously achieved in proton-proton colliders. Two general purpose detectors are built: the ATLAS and CMS detectors. Muons play a major role for discovery of new physics in the ATLAS experiment. It is therefore important to select the muons effectively in particular in the online trigger environment. To this purpose, a new tracking algorithm for precise reconstruction of muon momentum needs to be developed.

In this thesis, a new tracking algorithm for online muon reconstruction is presented. The algorithm utilizes the idea of Kalman Filter for taking into account non-uniform magnetic field provided for the muon spectrometer. The performance and the processing time of the algorithm was evaluated and compared to the existing algorithm. A significant improvement is observed in the momentum resolution.

Contents

List of Figures

Chapter 1

Introduction

The fundamental force in the nature is classified into four: electromagnetic, weak, strong and gravitational interactions. The Standard Model of particle physics is related to three among the four, namely, all but the gravity. The Standard Model has been very successful in describing the interaction between elementary particles in the framework of gauge theory. The theory is confirmed by many experiments for particle physics.

In the gauge theory, which is the base of the Standard Model, all gauge bosons are expected to be massless because of the gauge symmetry. In addition, quarks and leptons also should be massless under SU(2)×U(1) gauge symmetry . In reality however, most of the particles are massive. This is explained by the Higgs mechanism derived from the spontaneous symmetry breaking of the vacuum. The existence of the Higgs boson can prove correctness of the Higgs mechanism but it is the only particle which have been not discovered among particles in the Standard Model.

The LHC (Large Hadron Collider) constructed in Geneva, Switzerland is the largest proton-proton synchrotron collider in the world. Bunches of protons are accelerated up to 7 TeV and collide each other giving the center-of-mass energy of 14 TeV. The collisions rate is 40 MHz in order to achieve the high luminosity necessary for studies on rare interactions such as production of Higgs bosons or new physics beyond the Standard Model.

The ATLAS experiment is one of the multi-purpose experiments at the LHC. The most important goal of the ATLAS is to discover the Higgs boson. One of the most powerful method in discovering the Higgs boson is a search for a decay mode of $H \rightarrow ZZ \rightarrow$ 4-leptons(e, μ). Leptons with high transverse momentum (p_T) can be identified and the energy can be measured precisely in the ATLAS detector. This channel, therefore, gives a narrow peak in the four-lepton invariant mass spectrum over relatively small amount of background. In particular, the muons play a key role in the four-lepton channel because muon can be identified without backgroung. The ATLAS detector is designed to precisely measure of the muon momenta by using a combination of large volume air-coil toroid for the bending magnet and drift tubes with their location monitored by a dedicated alignment system.

At the LHC, the event rate will be high because the high intensity of the proton beam and the large cross section of proton-proton collisions. One of the keys for such an experiment is selecting the interesting events which include high p_T muons from W,Z bosons and new particles effectively. In the ATLAS experiment, three level triggers are provided for the selection. The level-1 trigger implemented on hardware, reduces the rate from 40MHz of bunch crossing rate to 75kHz. The level-2 trigger performs selection of events by running software processes on a PC farm. The rate is reduced from 75kHz to 3kHz. Then the selected events are sent to the Event Filter, the last stage of trigger system constructed on another PC farm. At this level, the trigger rate is reduced to 200Hz and remnant events are recorded.

The muon trigger selects events with muons of its p_T above a certain threshold. In the L2 muon trigger, the precise position information measured by the drift tubes can be used, whereas the L1 trigger can only a give rough position information. The L2 muon trigger performs more precise p_T measurement and severer algorithm than the L1 muon trigger. The rate of low p_T muons is expected to be high, because these muons are originated in the π and K particles in jets from the remnant quarks. The contamination of low-p_T muons mis-triggered as high-p_T muons causes increase of the trigger rate. Therefore, it is important to measure the p_T precisely to reduce by the low p_T muons in triggered events.

The TrigmuFast is provided at the first stage of the L2 muon trigger, and its role is to measure the p_T with the precise position information. It performs p_T measurement by using the bending angle in the magnetic field based on the curvature of the muon track. One of the important parameters for this calculation is the integrated magnetic field. But the integrated magnetic field varies position by position especially in the endcap region. Therefore, TrigmuFast calculates the p_T of a muon by using the measured its bending angle of trajectory and its position. The p_T is calculated by using a LUT method (Look Up Table) and parameters for the LUTs are prepared for segmented regions of the muon detectors. Thanks to the LUT method, the processing time of TrigmuFast is only 2 ms compared to 40 ms which is the limitation of the processing time for the L2 muon trigger.

TrigmuFast achieves the fast p_T measurement by measuring the bending angle and hit position. But it is difficult to measure the precise p_T when a particle passes through the area where the integrated magnetic field is close to zero. In addition, large multiple scattering angle causes mis-measurement of p_T. In this case, the method to reconstruct the track of a particle is effective for the precise p_T measurement. The Kalman Filter has advantages for these issues. It is originally introduced by R.E.Kalman in 1960, it has been applied for the reconstruction of particle in the experiments for particle physics. The Kalman Filter performs a fitting in the iteration between the prediction and the fitting parameters which describe the track of the particle at every measured position. With this procedure, a kink track, which can be seen in case of large multiple scattering, can be correctly reconstructed.

The aim of this study is introducing the development of a new fitting procedure using the Kalman Filter and a study of the performance with this new selection method. We have confirmed

that the improvement of the p_T resolution by using this new method. The averaged processing time with this new method is under the limitation of the processing time in the L2 muon trigger.

In the future, the LHC will be operated with a high luminosity. In such operations, the muon rate will be increased. By using this new method in the L2 muon trigger, it will be able to suppress the background events including low p_T muon, and to trigger the high p_T muons effectively

This dissertation consists of eight chapters. Chapter 2 and 3 introduce the LHC accelerator and the ATLAS experiment. In Chapter 4, an overview of ATLAS trigger system is presented. The performance of the L2 muon trigger is presented in Chapter 5. Introduction of Kalman Filter and the track fitting procedure is described in Chapter 6, and the performances with the new fitting method is presented in Chapter 7. The Chapter 8 is the summary of this study.

Chapter 2

The LHC experiment

2.1 The LHC accelerator

The LHC is the largest accelerator in the world. It was constructed at CERN (European Organization for Nuclear Research) located on the border of Switzerland and France. The LHC utilizes the tunnel originally prepared for the LEP (Large Electron-Positron) collider. The perimeter of this tunnel is 27km. The LHC collides two proton beams each other at a very high center-of-mass energy with a high frequency. The design center-of-mass energy is 14 TeV, which is the highest energy in the world. The synchrotron radiation of a proton is ten order of magnitude less than
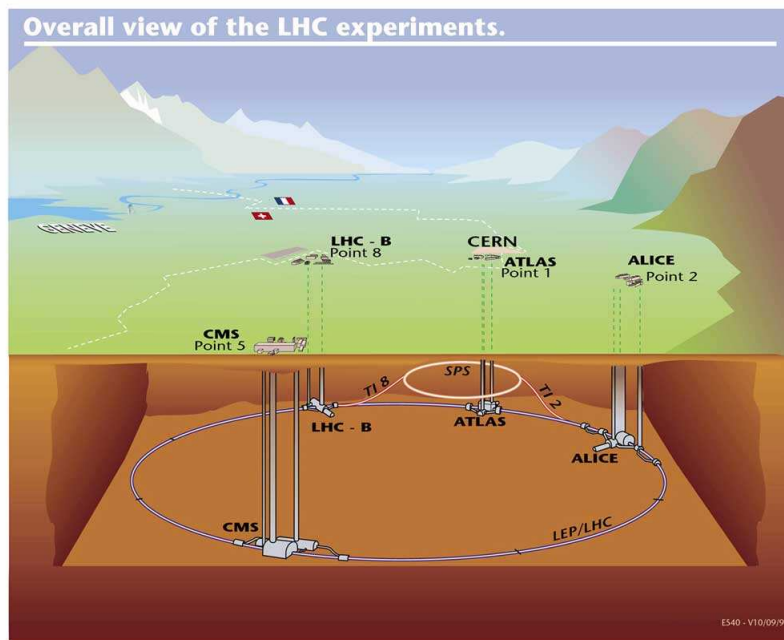

Figure 2.1: LHC and location of experiments

that of an electron at this energy. Therefore, the proton is only the choice for ring accelerators at this energy and radius. The proton has, however, the inner structure; it is composed of partons

which are quarks and gluons. This means that the effective center-of-mass energies of collisions of partons are much lower than 14 TeV. Nevertheless, it has a strong potential to find new physics at TeV energy scale. Another issue to be considered in proton-proton collisions is that the inelastic cross section between protons is very high (about a hundred of milibarn = 10^{-27} cm^2). A huge number of interactions occur and these events are the background for the new physics. Selecting the target physics events among such huge background events is the key of experiments at the LHC.

There are four collision points located in the LHC ring, provided for the following experiments.
- ATLAS (A Toroidal Lhc ApparatuS)
- CMS (Compact Muon Solenoid)
- LHC-b
- ALICE (A Large Ion Collider Experiment)

ATLAS and CMS are general-purpose detectors, LHC-b concentrates on the B-physics, such as rare decay or fine measurement of CP violation with B meson, and ALICE is a heavy ion collision experiment to study e.g. the nature of the quark-gluon plasma.

2.2 Physics Motivation

2.2.1 The Standard Model Higgs

The investigation of the dynamics responsible for the electroweak symmetry breaking is one of the most important tasks of particle physics. The Standard Model [1, 2, 3] of the electroweak and strong interactions is in very good agreement with almost all experimental measurements, but the dynamics, which is responsible for electroweak symmetry breaking, is still not experimentally proven.

Spontaneous symmetry breaking

In the Standard Model, the electroweak sector is described as a SU(2)× U(1) gauge theory, where all the electroweak interactions between fermions are described by exchange of massless vector bosons. The Lagrangian which describes the free vector boson field can be written as

$$\mathcal{L} = -\frac{1}{4}F_{\mu\nu}(x)F^{\mu\nu}(x) - \frac{1}{2}F^{\dagger}_{W\mu\nu}(x)F^{\mu\nu}_W(x) - \frac{1}{4}F_{Z\mu\nu}(x)F^{Z\mu\nu}(x), \tag{2.1}$$

By adding the terms, giving the masses to Z and W to the Lagrangian 2.1, it loses the invariance under the gauge transformation. To give the masses to the W and Z bosons while keeping the gauge invariance, a mechanism, called spontaneous symmetry breaking, is proposed.

To introduce the mechanism, suppose the Lagrangian density described in Eq. 2.2,

$$\mathcal{L} = \partial^{\mu}\varphi^*\partial_{\mu}\varphi - V(\varphi) \tag{2.2}$$

where φ is a complex scalar field and $V(\varphi)$ is the potential energy of the field. The actual forms of such terms are described as follows:

$$\varphi = \frac{\sqrt{2}}{2}[\varphi_1 + i\varphi_2], \tag{2.3}$$

$$V(\varphi) = \mu^2|\varphi|^2 + \lambda|\varphi|^4. \tag{2.4}$$

In Eq. 2.4, the constants λ and μ^2 are real with λ positive to make the total field energy bounded as described below.

It is required that the vacuum at the lowest energy state is invariant under the Lorentz transformations. This implies that $\varphi(x)$ is constant in this vacuum state. There are two possibilities for the vacuum state depending on the parameter μ^2. When μ^2 has a positive value, the minimum potential energy is realized at $\varphi = 0$. When μ^2 has a negative value, the minimum potential energy does not correspond to a unique value of φ but the value degenerate with the minimum lying on a ring in the complex plane. The value is described by Eq. 2.5.

$$\varphi V_{min} = \sqrt{\frac{-\mu^2}{2\lambda}}e^{i\theta},\ 0 \leq \theta \leq 2\pi. \tag{2.5}$$

As the Lagrangian in Eq. 2.2 is invariant under rotations in the complex plane of φ, each direction is equally good and setting $\theta = 0$ such that

$$\varphi V_{min} = \sqrt{\frac{-\mu^2}{2\lambda}} \equiv \frac{v}{\sqrt{2}} \tag{2.6}$$

can be done without loss of generality. A theory where the vacuum has less symmetry than the original Lagrangian is called a theory with spontaneous symmetry breaking.

The deviation from the chosen minimum can be described by the two real fields σ and η defined through

$$\varphi = \frac{\sqrt{2}}{2}[v + \sigma + i\eta] \tag{2.7}$$

The Equation 2.2 rewritten in terms of σ and η is then

$$\begin{aligned}\mathcal{L} = \frac{1}{2}\partial^\mu\sigma\partial_\mu\sigma - \lambda v^2\sigma^2 + \frac{1}{2}\partial^\mu\eta\partial_\mu\eta \\ - \lambda v\sigma[\sigma^2 + \eta^2] - \frac{1}{4}\lambda[\sigma^2 + \eta^2]^2 + c\end{aligned} \tag{2.8}$$

where the constant c is of interest only for general relativity. Taking the higher order terms as interaction terms the free Lagrangian reads

$$\mathcal{L} = \frac{1}{2}\partial^\mu\sigma\partial_\mu\sigma - \lambda v^2\sigma^2 + \frac{1}{2}\partial^\mu\eta\partial_\mu\eta. \tag{2.9}$$

It is seen that σ and η in fact are two real Klein-Gordon field. By quantizing these fields, Eq. 2.9 provides two different spin 0 particle fields. The σ bosons will have mass

$$m_\sigma = v\sqrt{2\lambda} \tag{2.10}$$

arising from the σ^2 term while the η bosons remains massless. The masslessness of the η bosons ia a direct consequence of the minimum being degenerate. The remaining terms in Eq. 2.7 can be treated as interactions among the σ and η particles.

Higgs mechanism

What is called the Higgs mechanism [4] is an application of the spontaneous symmetry breaking to create massive vector bosons in a gauge invariant theory [4, 5, 6]. Here it will be shown for a $U(1)$ theory. The idea is to replace the normal derivative in Eq. 2.2 with the covariant derivative:

$$D_\mu = \partial_\mu + iqA_\mu. \tag{2.11}$$

Adding the Lagrangian to the free gauge field A_μ results in

$$\mathcal{L} = D^\mu \varphi^* D_\mu \varphi - V\varphi - \tfrac{1}{4} F_{\mu\nu} F^{\mu\nu}. \tag{2.12}$$

This new Lagrangian is invariant under the $U(1)$ gauge transformation

$$\begin{aligned}
\varphi(x) &\rightarrow \varphi'(x) = \varphi(x) e^{iq\xi(x)} \\
A_\mu(x) &\rightarrow A'_\mu = A_\mu(x) + \partial_\mu \xi(x),
\end{aligned} \tag{2.13}$$

where ξ are any differentiable function. Continuing in exactly the same way as for the substitution with Eqs. 2.7 and 2.8 with a negative μ^2 and expressing the Lagrangian in terms of the variables σ and η as defined in Eq. 2.7, the result is

$$\begin{aligned}
\mathcal{L} = {}& \frac{1}{2} \partial^\mu \sigma \partial_\mu \sigma - \lambda v^2 \sigma^2 + \frac{1}{2} \partial^\mu \eta \partial_\mu \eta - \frac{1}{4} F_{\mu\nu} F^{\mu\nu} \\
& + \frac{1}{2} q^2 v^2 A_\mu A^\mu + qv A^\mu \partial_\mu + higher\ order\ terms
\end{aligned} \tag{2.14}$$

The Lagrangian clearly has a massive vector boson field A and two scalar fields σ, η with η massless, but unfortunately also a term $A^\mu \partial_\mu \eta$ which does not fit in. The Lagrangian 2.14 has one degree of freedom. The extra degree of freedom can be absorbed by choosing a specific gauge, where $\varphi(x)$ has the form

$$\varphi(x) = \frac{\sqrt{2}}{2} [v + \sigma(x)]. \tag{2.15}$$

Such a gauge transformation is always possible and the chosen gauge is called as the unitary gauge. In this gauge the η field disappears and the resultant Lagrangian is as follows;

$$\begin{aligned}
\mathcal{L} = {}& \frac{1}{2} \partial^\mu \sigma \partial_\mu \sigma - \lambda v^2 \sigma^2 - \frac{1}{4} F_{\mu\nu} F^{\mu\nu} \\
& + \frac{1}{2} q^2 v^2 A_\mu A^\mu + higher\ order\ terms.
\end{aligned} \tag{2.16}$$

Here the gauge boson can obtain non-zero mass by the term $\frac{1}{2} q^2 v^2 A_\mu A^\mu$. In summary, it is seen that a complex scalar field and a massless vector field, both with two degrees of freedom in Eq. 2.12 is transformed in Eq. 2.15 into one real scalar field with one degree of freedom and a massive vector boson field with three degree of freedom as a result of the Higgs mechanism. A massless spin 1 particle has two transverse polarized states while a massive spin 1 particle has an additional longitudinal polarized state. It should be noted that the η field only disappears if the η bosons

are massless. As shown in this section, this requires the vacuum state to be degenerate i.e. the Higgs mechanism will only work with a degenerate vacuum.

The Higgs mechanism is demonstrated here for a $U(1)$ gauge invariant Lagrangian. To extend it to $SU(2) \times U(1)$ gauge invariant Lagrangian of the electroweak theory, Lagrangian should contain a complex scalar doublet and four massless vector bosons. Counting degrees of freedom gives four from the scalars and eight from the vector bosons. Through the Higgs mechanism the Lagrangian is transformed into one real scalar, three massive vector and one massless vector bosons. The massless vector boson is of course to be identified as the photon and the single remaining scalar as the Higgs boson. Counting degree of freedom again gives one from the Higgs, two from the photon and nine from the massive vector bosons, again adding up to twelve.

The masses of the particles in the Standard Model are given as

$$m_H = \sqrt{2\lambda}v, \ m_W = \frac{1}{2}vg, \ m_Z = \frac{m_W}{\cos\theta_W} \tag{2.17}$$

where g is the weak coupling constant and θ_W the Weinberg angle. Using

$$v^2 = \frac{\sqrt{2}}{2G_F}, \ \alpha = \frac{g^2\sin^2\theta_W}{4\pi} \tag{2.18}$$

where G_F is the Fermi constant and α the fine structure constant, the vector boson masses can be expressed through G_F, α and $\sin\theta_W$. By using the Eq. 2.17, the vacuum expectation value is calculated

$$v = \frac{2m_W}{g} = 246 \ \mathbf{GeV} \tag{2.19}$$

Higgs boson production

The Higgs production processes at the LHC are shown in Fig. 2.2 and cross sections corresponding to these processes are shown in Fig. 2.3. More detail of each process is explained below.
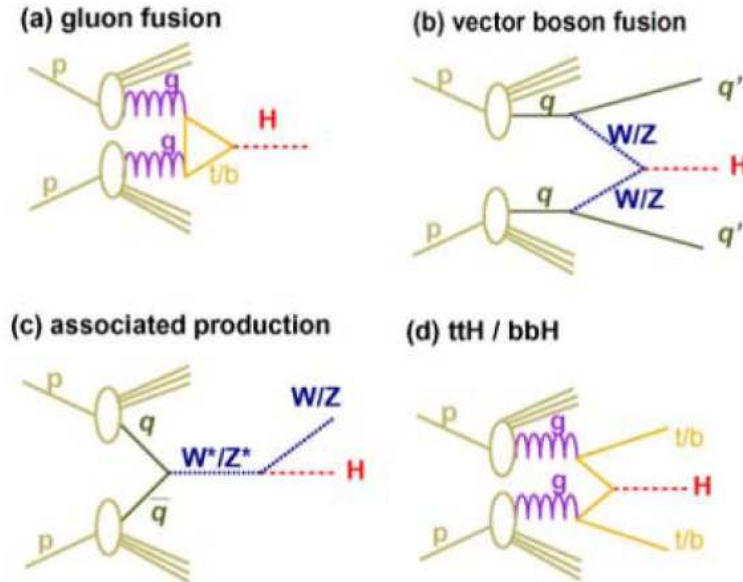
Figure 2.2: Feynman diagram of Higgs productions at the LHC.

Gluon fusion

In this process, the Higgs boson is produced through a loop of a top quark. This is the dominant process of the Higgs production at the LHC as shown in Fig. 2.3 because huge quantity of gluons are involved in p-p collisions. Since no associated particle characterizing the Higgs production is produced in the process, it is difficult to find the signal of the Higgs boson among the background events in this process.

Vector boson fusion

The event with this process has a characteristic signal: two high p_T jets in the forward regions and a rapidity gap between these recoil jets, which are effective for suppressing the background events.

Associated production with W/Z

The Higgs boson is produced through the bremsstrahlung of the W/Z bosons. The production cross section drops with increasing Higgs mass. The decay processes of $W \to l\nu$ and $Z \to ll$ are used to find this process among the background events.

Associated production with t/b (ttH/bbH)

The characteristic decays of associated two top(bottom) quarks are used for event selection.
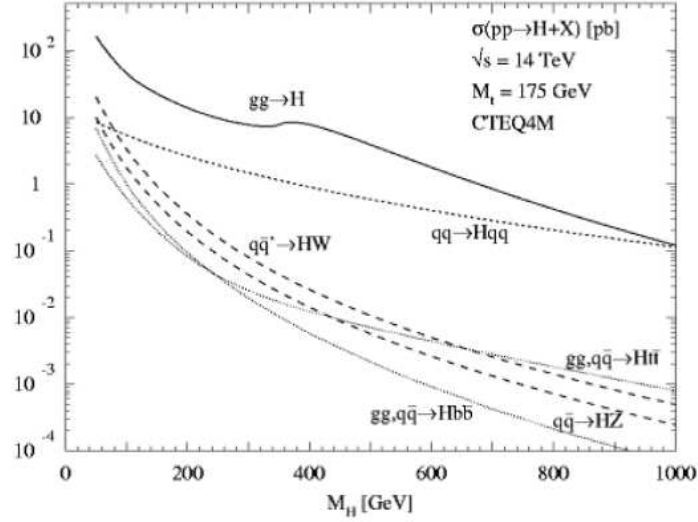
Figure 2.3: The production cross section of the Higgs boson at the LHC. The x-axis is the mass of the Higgs, and y-axis is the cross section of Higgs production [7].

This process is used for the measurement of the Yukawa coupling of top quark to the Higgs boson.

Higgs boson decays

Since the coupling of the Higgs boson to a particle in the Standard Model is essentially proportional to the particle mass, the Higgs boson decays predominantly to heavy particles and their branching ratios depend on the mass of the Higgs boson. Figure 2.4 shows the decay branching ratios of the Higgs boson as a function of its mass.
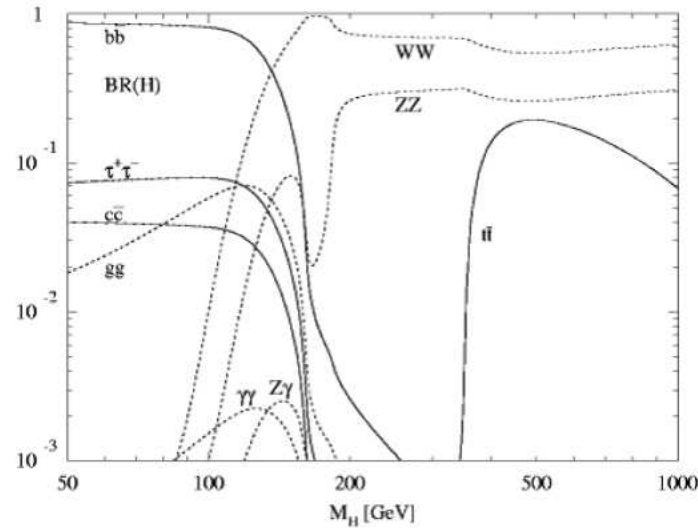
Figure 2.4: The decay branching ratios as a function of Higgs mass [7].

The region $m_H < 2m_W$

15

In this mass region, the major decay processes are the following:

$$H \rightarrow b\bar{b} \tag{2.20}$$

$$H \rightarrow \tau\tau \tag{2.21}$$

$$H \rightarrow \gamma\gamma \tag{2.22}$$

$$H \rightarrow WW^* \tag{2.23}$$

The dominant decay process is (2.20), but it is difficult to identify it at the LHC because of QCD background events. The energy resolution of b-quark is much worse than other particles as it is observed as one or more jets. The most promising process for the discovery of Higgs in this mass range is (2.22). Although the branching ratio of this process is small, it is possible to find a peak on backgrund events thanks to the high mass resolution ($\sigma \sim 1.4$GeV). For the VBF production, (2.21) is also an important decay process for discovery and (2.23) covers the wide range of the Higgs mass.

The region $m_H > 2m_W$

Figure 2.4 clearly shows that the decay to WW and ZZ is dominant in this region.

2.2.2   B-physics

At the LHC, enormous amount of B-hadrons are produced thanks to the large cross section for b-quark and high luminosity($L = 10^{33}$cm^{-2}s^{-1} at so-called low luminosity operation). With this large statistics, the precise measurement on the nature of B hadrons can be made. The aim of B-physics studies in the ATLAS experiment is to test the Standard Model through precision measurements of B-hadron decays, which may give indirect evidence for new physics, two of which are described below.

Measurement of asymmetry in $B_d^0 \rightarrow J/\psi K_s^0$

The measurement of the time-dependent CP-violating asymmetry of the decay $B_d^0 \rightarrow J/\psi K_s^0$ provides a clean measurement of the angle β of the unitarity triangle. To a good approximation, the Standard Model prediction for the asymmetry in this process is given by;

$$A(t) = \sin 2\beta \sin(\Delta m_d t), \tag{2.24}$$

where Δm_d is the mass difference in the $B_d^0 - \bar{B}_d^0$ system. The predicted symmetry is insensitive to the contribution from penguin diagrams. This makes the $B_d^0 \rightarrow J/\psi K_s^0$ decay the so-called gold-plated mode to measure the angle β.

In the final state of $B_d^0 \rightarrow J/\psi K_s^0$ process, J/ψ decays into muons or electrons. The $J/\psi \rightarrow \mu\mu$ process is detected as a cleaner signal than the process of $J/\psi \rightarrow ee$ in hadron-hadron collisions. Therefore, the muon system plays an important role for this study.

Rare decays of B meson

Certain rare decays, $B_{s,d} \to \mu\mu(X)$ for example, involve the flavor-changing neutral currents (FCNC) and are strongly suppressed in the Standard Model, with predicted branching ratios typically in a range $10^{-5} - 10^{-10}$. For the purely muonic decays, ATLAS will be sensitive to branching ratios of order 10^{-9} and should be able to measure the branching ratio for $B_s \to \mu\mu$ assuming the Standard Model prediction. New physics might result in significant enhancements over the Standard Model predictions.

Chapter 3

The ATLAS detector

ATLAS is a multi-purpose detector designed for precise measurements of p-p collisions at the LHC. Figure 3.1 shows the overall design of the ATLAS detector in 3D view. The size of the ATLAS detector is 22m in hight and 45m long along the beam axis. The coordinate system
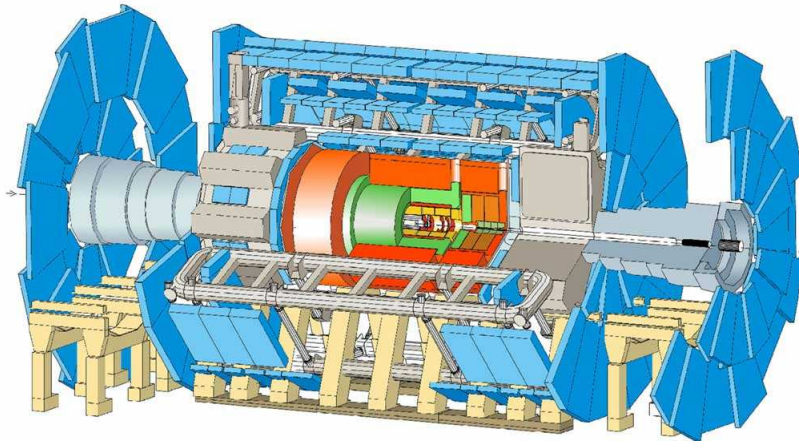
Figure 3.1: The ATLAS detector in 3D view[8]

of ATLAS is shown in Fig. 3.2. It is a right-handed coordinate system; the x-axis points to the center of the LHC ring and z-axis is set along the tunnel. The axis perpendicular to the z-axis is R giving the radius in cylindrical coordinate. The origin of this coordinate is set to the nominal interaction point. The region $z > 0$ is called A side and $z < 0$ is called C side. The pseudo-rapidity of particles from the nominal interaction point is defined as

$$\eta = -\log \tan \frac{\theta}{2} \tag{3.1}$$

where θ is the polar angle of the particle direction measured from the positive z-axis. The transverse momentum (p_T) is defined as the component of the momentum perpendicular to the z-axis.

Figure 3.2: Coordinate system of the ATLAS detector

The ATLAS detector consists of a magnet system and numbers of detector components. The detail of each component is explained in this chapter. Here a brief overview is given.

Magnetic fields are provided for identifying the charge and measuring the momentum of charged particles. The ATLAS detector 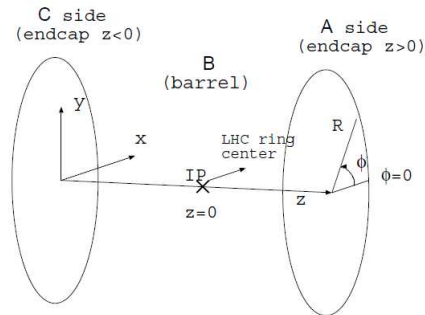has two types of magnets. One is a solenoid with its center at the nominal interaction point providing 2T magnetic field. The other is a system with toroids in the outermost part of the detector, giving magnetic field of 1-2T. The toroidal magnetic field is for measuring muon momentum and made with air-coil magnets to reduce multiple scattering. The combination of a long barrel toroid with two inserted endcap toroids makes the magnetic field covering up to $\eta = 2.7$.

The inner tracking detector, placed inside the solenoidal magnet, consists of Silicon-pixel vertex detector (Pixel), Semi Conductor Tracker (SCT) and Transition Radiation Tracker (TRT). The Pixel is placed closest to the interaction point and the SCT is located outside the Pixel, both of them surrounded by the TRT.

An electromagnetic calorimeter and a hadron calorimeter form the ATLAS calorimeter system. The electromagnetic calorimeter is a liquid argon sampling calorimeter, and it is placed outside the solenoid coil. The hadron calorimeter is a scintillator tile calorimeter for the barrel part, and placed outside the electromagnetic calorimeter. The endcap hadronic calorimeter is a liquid-argon type calorimeter.

The outermost part of the ATLAS detector is the muon system. Three layers of drift chambers are placed around the toroidal magnet.

3.1   Magnet system

Figure 3.3 shows the coils of magnets in the ATLAS detector. The coil located at the center of the ATLAS detector with a tube-like shape is the solenoidal magnet. The other coils are for toroidal magnets, the small ones are called "endcap toroidal magnets", and the long one is called "barrel toroidal magnets".
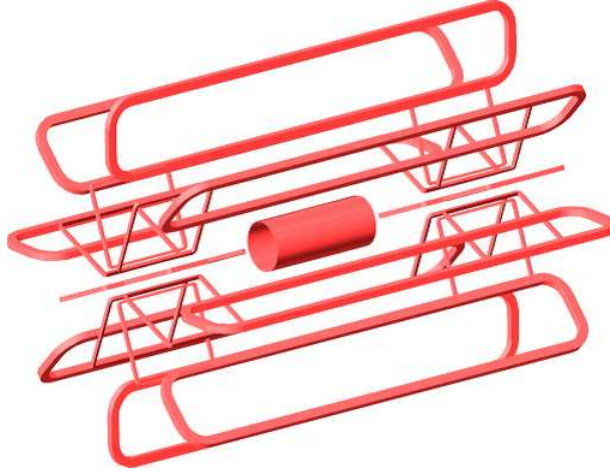
Figure 3.3: The coil of magnets in ATLAS detector.[9]

3.1.1 Solenoidal magnet

The solenoidal magnet is placed inside the electromagnetic calorimeter. This is kept at 4.5K in temperature. To reduce the amount of material, the magnet does not have a separate cryostat but rather it shares the cryostat with the liquid argon calorimeter located immediately outside. The magnetic field along the z-direction drops from 2T at the interaction point to around 0.5 at the end of the inner detector.

3.1.2 Toroidal magnet

The toroidal magnet system is divided into one barrel part and two endcap toroid systems. The integrated magnetic field along a particle track is the important factor for the momentum resolution. The structure is open with eight coils in the central region in separate cryostats. In the forward region, the toroidal field is also formed by eight superconducting coils.

By passing the two different toroidal magnets, the integrated magnetic field along the particle track has a position dependence in the forward region. Figure 3.4 shows the magnetic field at a layer in the x-y view. The circles in the figure represent the coil of troidal magnets, and lines are magnetic lines. It is clear that the interference of the magnetic fields from barrel and endcap toroids cause the complicated magnetic field. Figure 3.5 shows the integrated magnetic field as a function of η. Two curves, in red and black, show the integrated field at two different ϕ values. The difference of red and black lines comes from the measured position of ϕ. This graph also shows the complicated magnetic field especially in the endcap region($|\eta| > 1.0$). Such non-uniform magnetic field affects to the p_T measurement in the muon system. The details are described in following chapters.
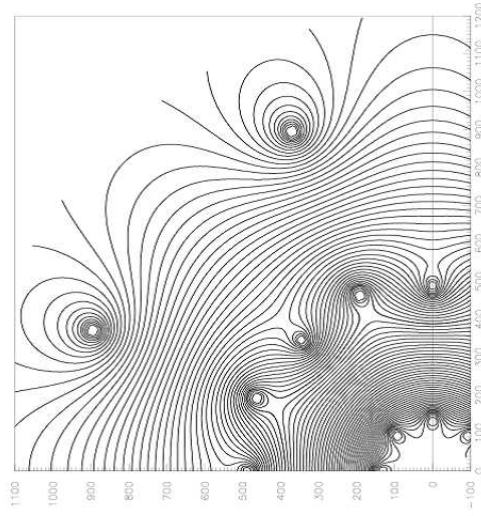
Figure 3.4: magnetic field map in x-y view. The lines indicates magnetic lines.
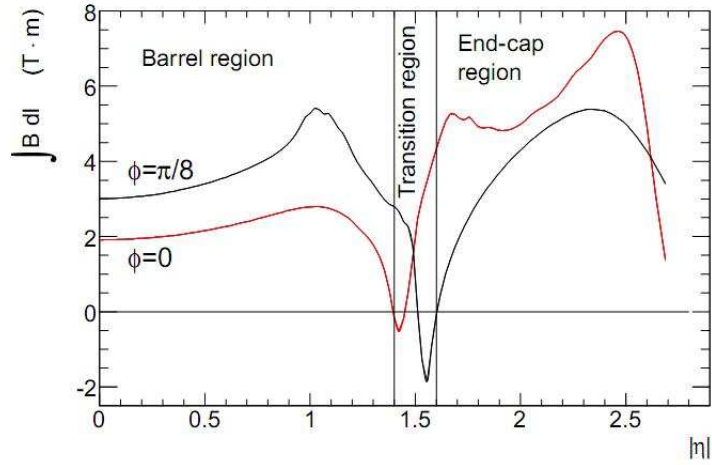

Figure 3.5: Integrated magnetic field provided by the toroidal magnet system in the ATLAS detector.

3.2 Inner detectors

The innermost part of the ATLAS detector is dedicated to tracking charged particles. It can reconstruct the tracks of charged particles precisely with finely segmented detectors in the magnetic field of the solenoid. The layout of the ATLAS inner detector is shown in Fig. 3.6. The most important points for the inner detector are as follows.
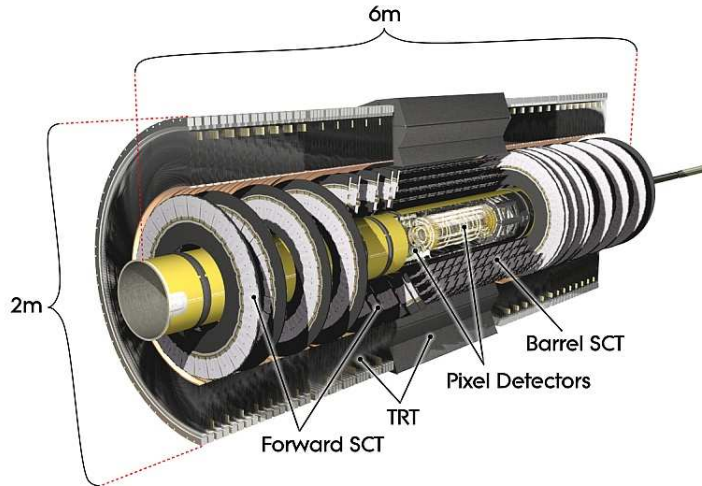
Figure 3.6: The overall view of the ATLAS inner detector in 3D [8].

- Identification of individual particles in dense jets where the calorimeter cannot resolve the individual particles. At the same time, the rate of fake tracks should be low.

- Momentum measurement in a large momentum range. Below a transverse momentum of 0.5 GeV, the particles loop in the magnetic field, making the pattern recognition very difficult. This lower limit affects the reconstruction of converted photons and J/ψ decays.

- Charge identification of particles with large transverse momentum for the identification of e.g. a possible Z′ decay. Increasing the magnetic field will improve the charge identification but at the same time increase the p_T limit for loopers.

- Distinguish between electrons and photons, which create similar clusters in the electromagnetic calorimeter.

- Decay length reconstruction for CP-violation studies in the B-system and for B_s^0 mixing measurement.

- Tagging of jets originating from high energy b-quarks. The b-jets can be from a $H \rightarrow b\bar{b}$ decay or decays of supersymmetric particles. The tagging is done by secondary vertex identification and through the identification of leptons from semileptonic B-meson decays.

- Electron/jet separation in addition to the separation already provided by the calorimeter.

- Momentum measurement of low energy muon which have large multiple scattering in the hadron calorimeter.

- Identification of the primary vertex in the presence of many vertices from overlying minimum bias events.

In line with the coverage for the detection of electrons and muons in the calorimeter and muon system, the coverage of the Inner detecter extends up to $|\eta| <2.5$.
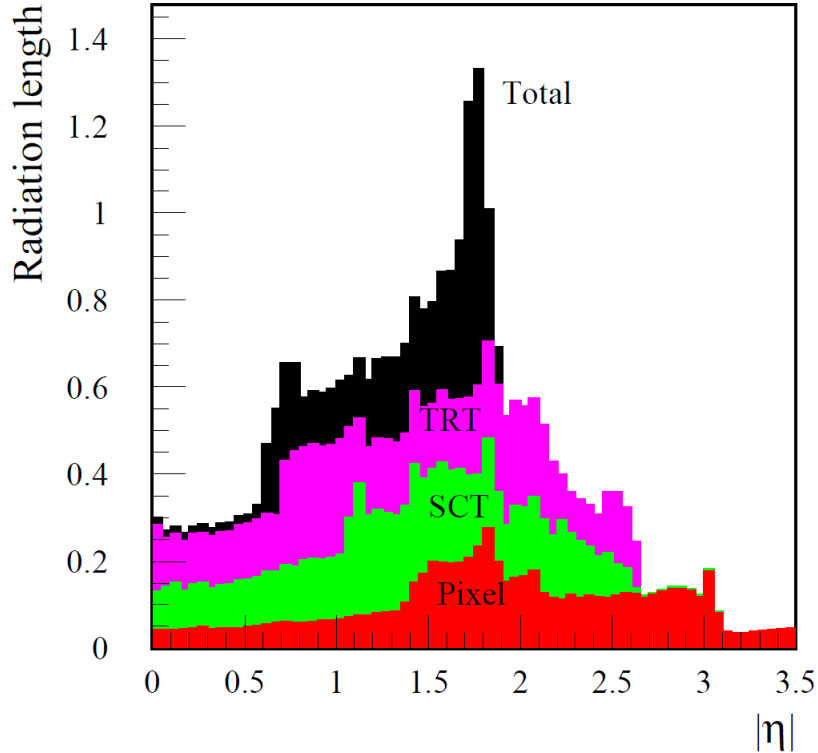
Figure 3.7: the distribution of Radiation lengths in the inner detector.

It is important to keep the amount of material in the inner detector low. The material budget for the inner detector is shown Fig. 3.7. Photon conversions, bremsstrahlung from electrons and nuclear interactions with pions all cause a degraded calorimeter performance. The large track density, however, requires detection elements with a fine granularity.

3.2.1 Silicon-Pixel detector

The pixel detectors have fine detecting elements of size 50μm $\times$ 400 μm thus giving a 2-dimentional coordinate with just one layer. The better resolution is in the φ coordinate. Figure 3.8 shows the layout of the Pixel detector.

The most important requirements for the pixel detectors are to provide secondary vertex information for full reconstruction of B-meson decays, such as b-tagging in top physics, a $H \to bb$

Figure 3.8: A 3D view of the ATLAS Pixel detector.[8]

decay and possible decays of supersymmetric particles. For better performance in reconstructing secondary vertices, the first pixel layer has to be as close as possible to the beam pipe.

3.2.2 Semi-conductor tracker

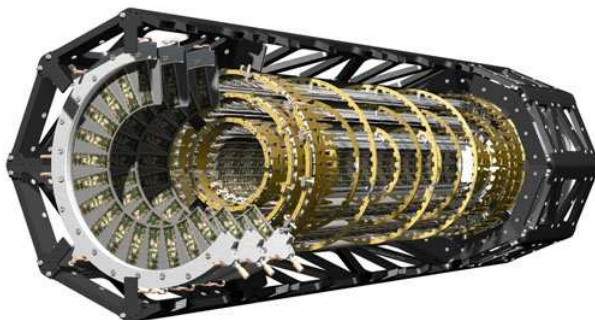The silicon strip detectors have an n-type bulk with a single sided readout of n+ strips. Although radiation damage will cause the bulk material to change into a p type semiconductor with time, the detectors will still be functional. In each of the layers of the detector, two single sided detectors are placed back to back. For one of the layers the strips are parallel to the beam pipe thus measuring the φ coordinate directly. The strips on the back side are rotated by 40 mrad to give a stereo view and thereby reconstructing the $z(R)$ coordinate in the barrel (endcap). Each strip in the detecting element will have a length of 12 cm and a width of 80 μm.

3.2.3 Transition radiation tracker

The Transition Radiation Tracker (TRT) is placed between the silicon tracker and the solenoid. The TRT consists of thin proportional chambers, either in the form of straws with fibers embedded or with foils and straws in separate layers.

In total there are around 370000 straws with 4mm diameter in the TRT, which are placed radially in the endcap and along the beam axis in the barrel region.

The straws are filled with a Xenon gas mixture (70%Xe, 27%CO_2, 3%O_2). Xenon is used for the absorption of transition radiation. CF_4 enables the gas to have a faster drift-time for electrons, providing higher spatial resolution and reducing the influence from neighboring bunch crossing at the LHC. As a (Xe/CF_4) gas mixture is not stable under high voltage, CO_2 is added to stabilize the gas, thus preventing sparks and streamers inside the straw during operation. In the center of the straw is a 30 μm gold covered tungsten wire. The gas gain in the straws will be 2.5×10^4 and the total drift-time approximately 40 ns and thus not fully contained within one bunch crossing.
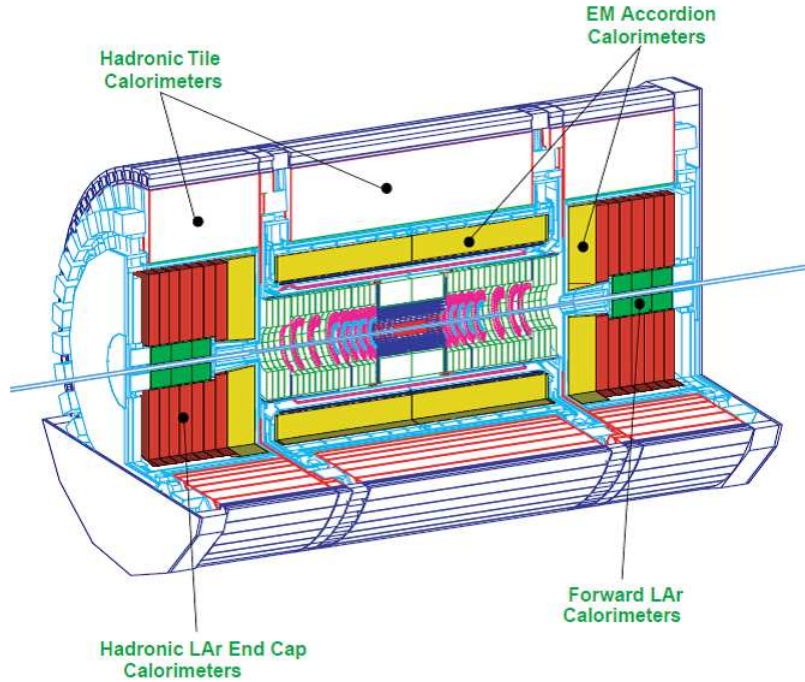
Figure 3.9: A 3D-view of the ATLAS calorimeter system.[10]

3.3 Calorimeters

A calorimeter is almost always divided into an electromagnetic and hadronic calorimeter. The distinction is possible because of the different interaction behavior between electrons/photons and hadrons. The ratio between the response of the calorimeter for the purely hadronic and purely electromagnetic part of the shower is called the e/h ratio. For a good energy resolution the value of e/h should be as close as possible to one. The size of hadronic showers depends linearly on the interaction length λ of the material which is always longer than the radiation length.

A measurement of missing transverse energy is a way to measure particles escaping the detector without interactions. This can either be neutrinos or stable supersymmetric particles. To identify missing transverse energy, the calorimeter needs to have a good hermeticity. This means that the rapidity coverage has to be extended as forwards as possible and any cracks in the detector for cables and cooling have to be minimized. The hadronic calorimeter also needs to be thick enough to avoid leakage of hadrons into the muon system, which would both degrade the resolution in missing transverse energy and give background in the muon system.

3.3.1 Liquid argon calorimeters

The electromagnetic calorimeter in ATLAS is a liquid argon sampling calorimeter. The lead/stainless steel is used for layers and liquid argon are interspaced. The lead gives the shower development with its short radiation length and the secondary electrons create ionization in the narrow gaps of liquid argon. An inductive signal from the ionization electrons drifting in the

electric field across the gap is registered by copper electrodes.

To achieve a low capacitance of the detecting elements and thereby a fast signal, the lead plates have an accordion shape shown in Fig. 3.10. At the same time, this creates a fully homogeneous
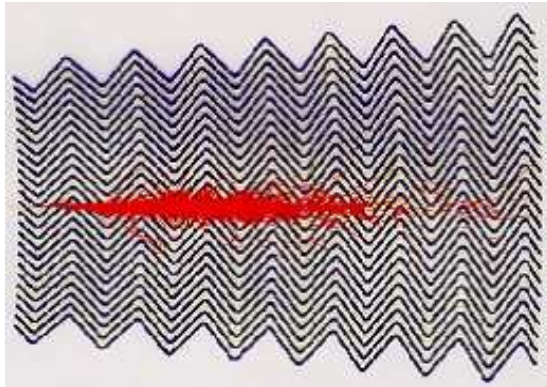

Figure 3.10: Schematic view of a shower in the Liquid Argon Calorimeter.[8]

structure in the φ coordinate.

The endcap electromagnetic calorimeters start at $|\eta|$=1.5 and continue down to $|\eta|$=3.2 but with an increased cell size above $|\eta|$=2.5. There is a crack with degraded energy resolution where the endcap and barrel calorimeters meet. The resolution of the electromagnetic calorimeter is described by Eq. 3.2 with energies measured in GeV.

$$\frac{\Delta E}{E} = \frac{11.5\%}{\sqrt{E}} \oplus 0.5\% \tag{3.2}$$

To withstand the high radiation levels in the forward region, the hadronic calorimeter is also of liquid argon type in the endcaps. The design is simpler than the electromagnetic calorimeter and has parallel copper plates as absorbers placed perpendicular to the beam. The very forward hadronic calorimeter with a coverage down to $|\eta|$=4.9 is made of copper/tungsten. The choice of copper/tungsten is necessary to limit the width and depth of the showers from high energy jets close to the beam pipe, and to keep the background level low in the surrounding calorimeters from particles spraying out from the forward region. The calorimeter is a metal matrix with cylindrical holes. The holes have rods inside with a slightly smaller radius allowing for liquid argon gap of just 250 μm.

3.3.2 Tile Calorimeters

The hadron calorimeter of the ATLAS detector is a tile calorimeter which covers the central region reaching $|\eta|$=1.7. The tile calorimeter is a steel matrix with scintillators inserted as tiles as shown in Fig. 3.11. The scintillator tiles are placed such that the shower passes through them from the side to improve the e/h ratio.

The light created in the scintillator tiles is read out with wavelengh shifting fibers to photo-multipliers, placed on the outside of the calorimeter. The fibers absorb the blue light from the
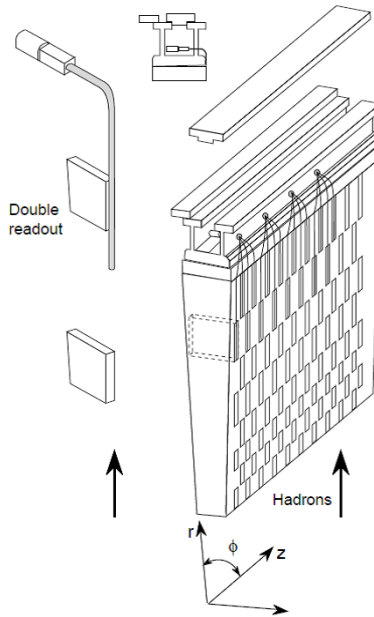
Figure 3.11: A part of tile calorimeter.[13]

scintillators and re-emit it at longer wave-lengths where it reaches the photo-multipliers through total reflection inside the fibers.

The resolution of the hadronic calorimeter is

$$
\begin{aligned}
\frac{\Delta E}{E} &= \frac{50\%}{\sqrt{E}} \oplus 3\% \qquad for \ |\eta| < 3 \\
\frac{\Delta E}{E} &= \frac{100\%}{\sqrt{E}} \oplus 10\% \qquad for \ 3 < |\eta| < 5
\end{aligned}
\tag{3.3}
$$

where the constant term is dominated by the different response to the hadronic and electromagnetic part of the shower as a larger part of the total energy ends up as an electromagnetic shower at high energies.

3.4 The muon system

The identification of muon is important for an experiment working at a high energy p-p collider. The general layout of the muon system is shown in Fig. 3.12. The muon system consists of two types of detectors on its purpose. One is the trigger chambers to select events with high energy muons and the other is the precision chamber to measure the precise position.

3.4.1 Trigger chambers

Two types of trigger chambers are placed in the muon system, one is Resistive Plate Chamber (RPC) covering $|\eta| < 1.05$ and the other is Thin Gap Chamber (TGC) for $|\eta| > 1.05$.
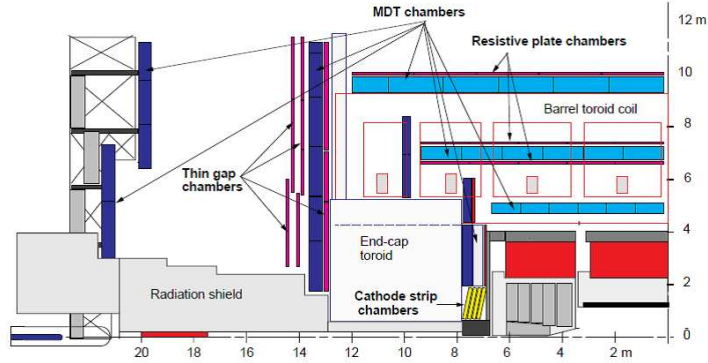
27

Figure 3.12: A layout of muon chambers in the ATLAS experiment.[14]

The RPC has a gas-gap between two resistive bakelite plates with metal strips. The gas used for the operation is mixed one (94.7%$C_2H_2F_4$, 5%Iso-C_4H_10, 0.3%SF_6). A uniform electric field between the plates creates avalanches when a particle passes the gas-gap and the induction from the avalanche is measured by the closest metal strip. The 2 mm-thick gas-gap gives a fast detection with a 1 ns time resolution allowing the individual bunch crossings to be identified. The metal strips on each side of the detector are perpendicular to each other giving a position resolution of 1 cm in each plane.

TGC has a similar structure to the multi-wire proportional chamber (MWPC), and it is operated in the saturated mode. This chamber has 2-dimensional readout from wire as anode and strip for cathode. The basic structure is the gas volume, which are sandwiched by two graphite cathode planes and 50μm wires spaced every 1.8 mm in this volume. The cathode plane is made of a 1.6 mm FR4 plate on which the graphite is deposited. Behind the interior cathode plane, etched copper strips provide the readout. A mixed gas are used in the operation, and the ratio is (55%CO_2,45%n-C_5H_{12}). Figure 3.13 is a cross section view of the TGC.
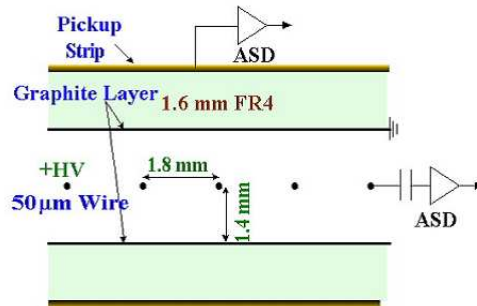

Figure 3.13: A cross section view of TGC [10].

The region between the graphite layers are fulfilled with the mixed gas. When a charged particle passes through such a gas volume, the gas molecules are exited by the particle and emit electrons. With high voltage provided between the wire and graphite layer, the emitted electrons drift in the gas volume to the anode and are detected.

28

3.4.2 Precision chambers

To measure the precise position of the particles passing the muon system, Cathode Strip Chamber (CSC) and Monitored Drift Tube (MDT) are placed in the muon system. The MDT is proportional chambers made of alminium tube of 30 mm diameter and lengths varying from 70cm to 630cm. In the operation, the mixed gas of the argon and CO_2 is used. The ratio is (93%Ar, 7%CO_2) A general MDT chamber used in the ATLAS detector is presented in Fig.3.14.
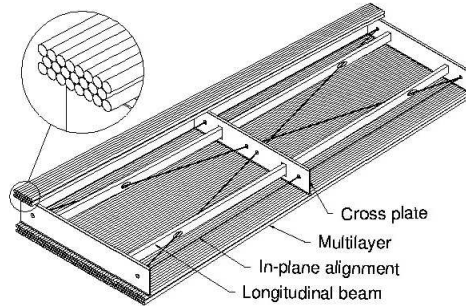

Figure 3.14: A picture of MDT chamber.[10]

To measure the coordinate in the bending plane of the magnet, the tubes are placed transverse to the beam axis. A set of MDT's consists of 2 superlayers, each with 3 or 4 layers of tubes. Such many tubes in each set are required to reduce the level of fake tracks reconstructed from random associations of background hits and to provide 100% efficiency for each set.

The detection principle of the MDT is following. As described above, the MDT consists of layered drift tubes. When a charged particle passes through a tube, the gas molecules are ionized along the trajectory. The ionized electrons drift to the wire of the tube and the signal induced from the electrons and ions is read out. The drifted length is calculated by pre-determined the relation between the drift length and the drift time. The drift length from the wire of the tube can be treated as the radius of a circle. Therefore, by fitting the drift circles in multi layers in MDT chamber with a straight trajectory tangent to the circles, the path of the particle is reconstructed.

The MDT's are not used in the forward region because of their long tubes resulting in a too high rate. Instead the CSC is placed close to beam pipe covering is $2.0 < |\eta| < 2.7$. The CSC is multi-wire proportional chambers with a wire spacing of 2.5mm. Cathode strips arranged perpendicular to the anode wires give the second coordinate in the readout which, together with the much finer granularity compared to the MDT's, make it possible to find tracks in the forward region, where the track density is higher than the barrel region.
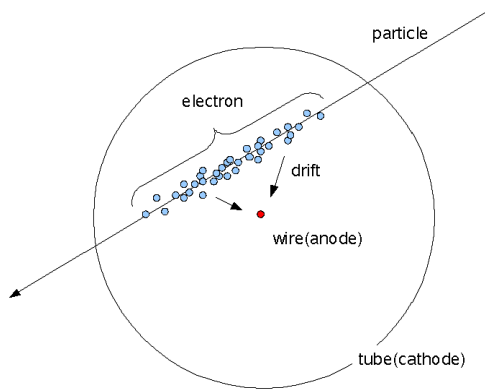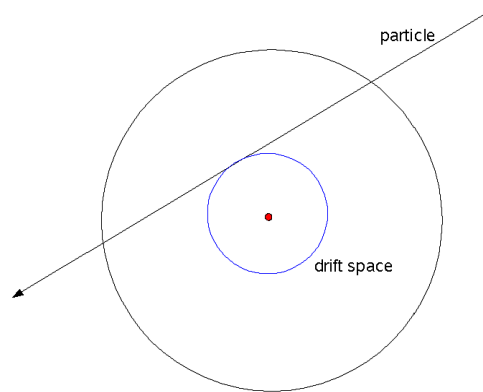
Figure 3.15: MDT principle

Figure 3.16: drift space

Chapter 4

The ATLAS trigger system

At the LHC, the interaction rate of protons at the design luminosity is expected to be about 1GHz. The trigger system is required to select interesting events effectively among enormous amount of such background events.

Figure 4.1 shows a schematic view of the trigger and data flow system of the ATLAS experiment. The trigger system is three-leveled triggers: Level-1 (L1), Level-2 (L2) and the Event Filter (EF). The L1 trigger is implemented using custom-made electronics for calorimeters and the muon detectors. Selections of L2 and EF are based on software algorithms processed on a PC farm where the information of the inner detector is also available. The L2 and EF form the high-level trigger (HLT) together with the event builder. The data from collisions in every detector are temporary kept in the pipe-line memories until L1 decision are made. Then the data corresponding to the collision are read out through the Read Out Drivers (ROD) and sent to Read Out Buffers (ROB), which is a part of the Read Out System (ROS). At the HLT, network switches are used to transfer the data between the PC nodes. The maximum trigger rates at L1, L2 and EF are 75~kHz, 3~kHz and 200~Hz, respectively.
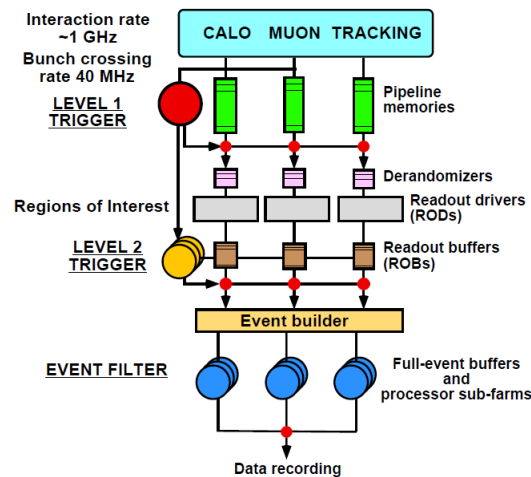

Figure 4.1: Block diagram of the Trigger and DAQ system[11]

4.1 Overview

4.1.1 The Level-1 trigger

When a particle passes through detectors, interactions between the particle and materials are converted into electronic signal and digitized. In the ATLAS experiment, the digitized signals are kept until the L1 decision arrives at pipe-line memories, called "Level-1 buffer", equipped in the front-end electronics of every detector system. A block diagram of L1 trigger is shown in Fig. 4.2.
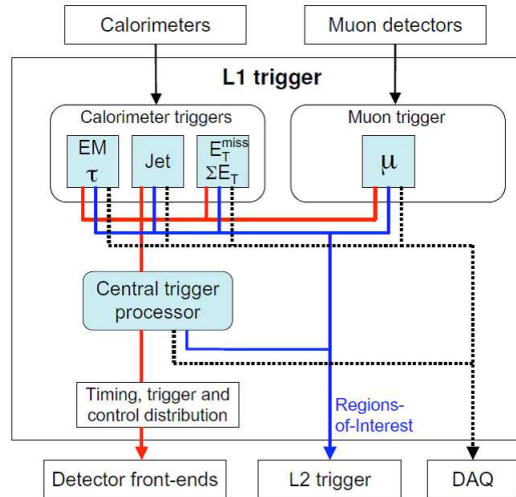

Figure 4.2: A block diagram of L1 trigger[15]

The L1 trigger consists of two subtrigger systems. The muon trigger searches high-p_T muons and the calorimeter trigger identifies features with high-E_T objects like electrons, photons, jets and τ-leptons decaying into hadrons. The calorimeter trigger also selects events with large missing E_T and large total E_T. After these selections, the L1 Accept is made by the Central Trigger Processor (CTP), which combines results from muon and calorimeter triggers. The L1 accept is distributed to the front-end electronics via the Timing, Trigger and Control (TTC) system. The latency of the L1 trigger, which is defined as the interval between the collision of protons and arrival of the signal of L1 accept to the front-end electronics, is 2.5 μs. Once the L1 accept is delivered, the data kept in pipe-line memories are read out and sent to the ROB through Read Out Links (ROL's). In order to effectively perform L2 algorithm within a limited time, the region of interest (RoI) information, indicating the area of detectors where positive signals are observed at L1, is produced. RoIs are created in the sub-systems of L1 trigger (muon, calorimeters and CTP) and sent to the L2 trigger.

4.1.2 High-level trigger

The HLT consists of the L2 trigger, the EF and the event builder in between L2 and EF. The L2 trigger applies more sophisticated algorithms than that in the L1 trigger using the data associated to RoIs. The L2 trigger system is implemented in a PC farm. The maximum processing
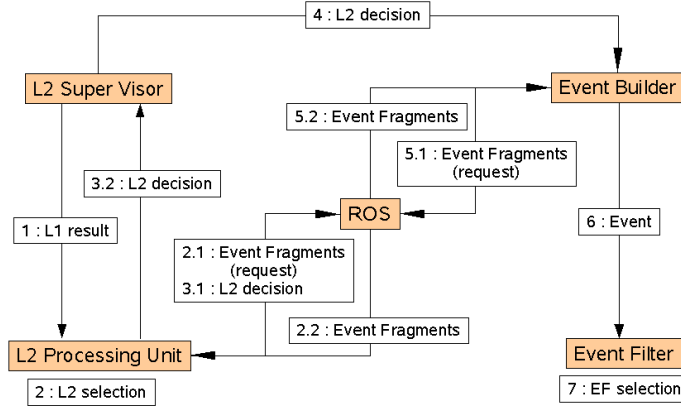
time allowed for each event is 40ms.

Figure 4.3: A flow chart of the data and triggers between the functional blocks of HLT. The numbers on the line between boxes indicate the order of processing of trigger.

The logical structure of the HLT consists of several functional blocks: the RoI builder, the L2 SuperVisor (L2SV), the L2 Processing Unit (L2PU) and the L2 trigger-specific ROS (pseudo-ROS). The role of the RoI builder is to assemble the RoI information sent from the different sources in L1 trigger into a single data structure, called the RoI record, which is sent to the L2SV. The L2SV controls data and message flow in the L2 trigger system. Figure 4.3 shows a flow chart between functional blocks of the HLT. The L2SV assigns one of the L2PUs to process an event by using the data associated with the RoI record. When a L2PU receives the RoI information from the L2SV, it requests corresponding data to the ROS of the detector of interest. Then it performs algorithms for selecting event. The results are sent to the pseudo-ROS, a software component behaving like real ROS. The pseudo-ROS adds the detailed LVL2 results into the event data. The result of the selection is sent back to the L2SV.

When an event is accepted by the L2 trigger, the Event Builder collects and assembles full data from all the detectors. The Event Builder consists of DFM (Data Flow Manager), ROS and SFI (Sub Farm Interfaces). The DFM is a multi-thread application supervising event building processes. When the DFM receives the result of the selection by the L2 trigger, it asks the SFI to collect all the data in the event from the ROS and to assemble them. The SFI informs the completion of event building to the DFM. Then the DFM asks to the ROS to clear the data after the event is built or the event is rejected by the L2 trigger.

The EF performs selection algorithms after the standard ATLAS reconstruction and analysis applications. The data from all part of the detectors can be used for the selection. The limit on the processing time is 4s per event. At the EF the event data accepted in the selection criteria are classified into pre-determined sets of so-called event streams, such as electrons, muons, jets,

photons, E_T^{miss} and τ, and B-physics. The flags indicating the classification is added to the event structure. The event data are sent to the SFO (Sub Farm Output) and are recorded in a mass storage system.

4.2   Muon trigger

The L1 muon trigger selects events with high-p_T muons for every bunch-crossing. The selected muons by the L1 trigger are either confirmed or rejected by using accurate reconstruction of muon trajectory in the HLT (muon HLT).

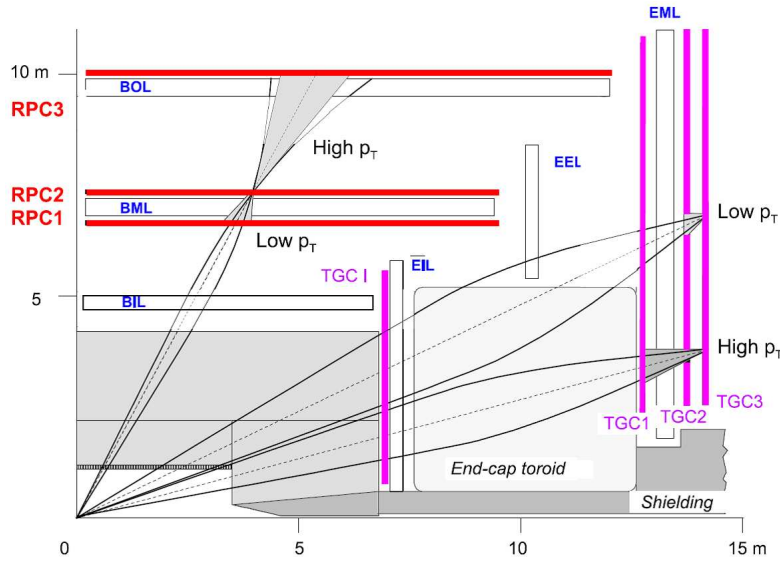### 4.2.1   Level-1 muon trigger

Figure 4.4: A layout of L1 muon trigger system [15]

The L1 muon trigger is based on finely segmented trigger chambers located in the outer region of the ATLAS detector, the RPC for barrel region ($|\eta| < 1.05$) and the TGC for the end-cap region ($1.05 < |\eta| < 2.4$). Figure 4.4 shows locations of these chambers and typical trajectories of muons. High p_T muons are selected in the barrel and endcap regions independently. The detail of the selection method is described in the following.

The principle of the selection method in the L1 muon trigger is making coincidences of hits in multi-layered chambers, measuring the p_T quickly by calculating bending angles and classifying the tracks into six intervals in p_T. The p_T is measured in three steps. The first step is the determination of a trajectory with infinite momentum, the second is the measurement of the deviation between hits and infinite momentum trajectory, and the last step is the selection of the p_T intervals to which the muon belongs by estimating its p_T value from the deviation. The relation between the deviation and the p_T intervals is given by a look-up tables (LUT). These

LUTs are made from a Monte-Carlo simulation of single muon events. Muon candidates found in the barrel and endcap regions are sent to the Muon to Central Trigger Processor Interface (MUCTPI) with the p_T class. The MUCTPI combines all the L1 muon trigger information and count the number of muon candidates for each of six p_T intervals. The MUCTPI also removes double count of a muon by taking into account overlapped detector regions.

4.2.2 L1 barrel muon trigger

The RPC chambers in the barrel region are organized in three layers. The inner two layers, RPC1 and RPC2 in Fig. 4.4, are located at approximately 7.5m from the beam axis. This location is called Barrel Middle (BM) station. The third layer, RPC3, is located in the outermost of the Barrel Outer (BO) station located at about 10m from the beam axis. Every layer is made of a doublet chamber with two gas gaps. There are two types of chambers in each layer, large chambers for large sectors and small chambers for small sectors, as shown in Fig. 4.5.
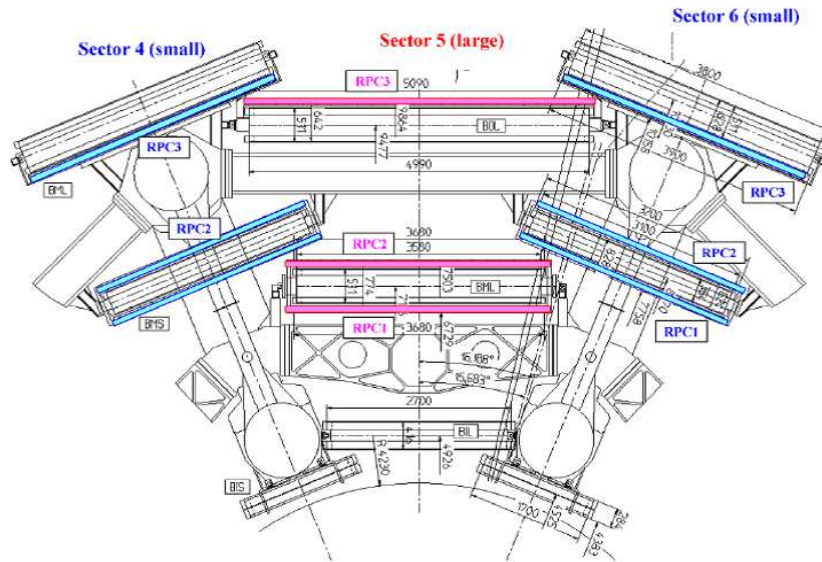
Figure 4.5: A part of the cross section view (in x-y plane) of the barrel muon system [15].

The RPC measures hit positions in η and ϕ coordinate. The particle is bend in η direction in the barrel toroidal magnets. Avoiding dead area, the sensitive areas are overlapped with adjacent chambers for both in η and ϕ direction.

Muon tracks pointing to the nominal interaction point are searched in two phases of coincidences, called low-p_T and high-p_T triggers. The low-p_T trigger is processed in the following way. When a hit is observed in RPC2 (pivot plane), hits in the RPC planes are searched within a road from the hit in the pivot plane. The road is defined as a region within a certain width from the straight line drawn from the nominal interaction point to the hit in the pivot plane. The width of the road is determined from the angle of the lowest p_T tracks in consideration. Three hits

Figure 4.6: The Road for high-p_T and low-p_T trigger in the L1 barrel muon trigger [15]

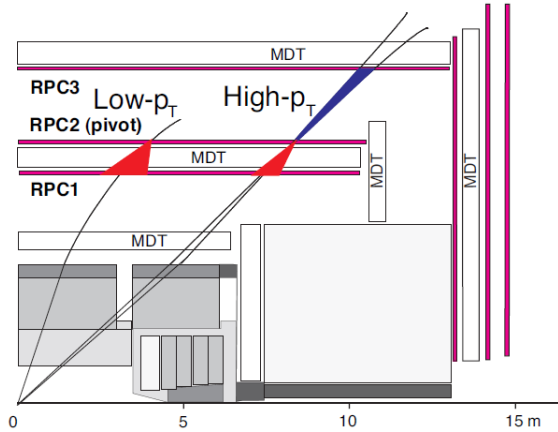are required for the four detector gaps in RPC1 and RPC2 for the low-p_T trigger. The hits in a road are grouped and used to determine the local angle and position of a so-called "tracklet". Deviations of hits found in a road from the infinite momentum track are measured and used to determine the p_T by using the LUT.

For the high-p_T trigger, RPC3 is used in addition to the RPC1 and RPC2. Expect for the width of the road, the selection method of high-p_T trigger is similar to that low-p_T trigger. As for the coincidences of chambers, one hit in two chamber gaps in the RPC3 is required in addition to the 3-out-of-4 coincidence in the low-p_T trigger. Deviations of muons both in η and ϕ are calculated in parallel. They are combined to determine the p_T.

The RPC L1 data are segmented as follows. The largest division is $\eta < 0$ and $\eta > 0$. The half of the barrel system consists of 16 sectors, eight for small and eight for large chambers. All the chambers are divided in two in ϕ direction, giving large or small trigger sectors. As a result, a half of the barrel is divided into 32 trigger sectors. Further segmentations, called Pad and RoI, are shown in Fig. 4.7. Each sector includes 7 Pads for trigger large sectors and 6 Pads for trigger small sectors. The size of each Pad is 0.2×0.2 in $\Delta\eta \times \Delta\phi$. A Pad includes 4 RoIs, each of which covers the area of about 0.1×0.1 in $\Delta\eta \times \Delta\phi$. The total number of Pads is 832 and there are 3328 RoIs.

4.2.3 L1 endcap muon trigger

The TGC chambers are used for the L1 trigger in the endcap region. The TGC consists of four layers, each of which is called, from the nominal interaction point to outside, TGC EI/FI, TGC1, TGC2 and TGC3. The chambers are placed perpendicular to the beam axis. The EI/FI layer is located at about 7m from the nominal interaction point in z, and the others are located at about 14m. The coverage of the TGC are $1.05 < |\eta| < 2.4$ for the TGC1, TGC2 and TGC3, and $1.05 < |\eta| < 1.96$ for the EI/FI. A TGC chamber has a two-dimensional readout; the wire
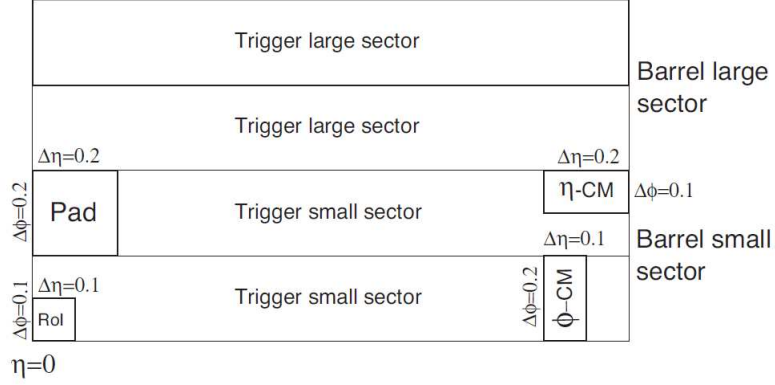
36

Figure 4.7: The division of Pad and RoI in the sectors. CM stands for Coincidence Matrices for identifying the p_T of a muon [11].

gives R direction and the strip gives the azimuthal angle ϕ. TGC EI/FI, TGC2 and TGC3 are doublet chambers with two detector gaps. TGC1 consists of triplet chambers with three detector gaps. A doublet chamber has two readout layers for both wire and strips. A triplet chamber has three readout layers for wires and two readout layers for strips. The pivot plane of the L1 end-cap muon trigger system is TGC3, the outermost layer.
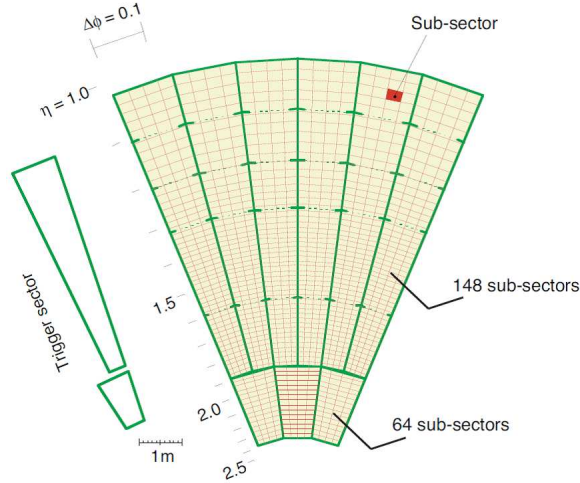
Figure 4.8: Readout and trigger sectors in an TGC octant [11]

The end-cap muon system is subdivided into eight parts in ϕ, called octant, which is shown in Fig. 4.8. A wheel is divided in two regions: "endcap" corresponds $|\eta| < 1.92$, and "forward" is $|\eta| > 1.92$. The endcap part of octant is divided in six in ϕ and the forward is divided in three, called sectors. A sector is divided into RoIs, the number of which is 148 (64) for an endcap (forward) sector.

When a hit is found in the pivot plane, the deviations of hit positions in other planes are calculated. Here the deviation is defined as the distance, in R and ϕ, between the hit and the line connecting the hit in the pivot plane and nominal interaction point. These deviations are used to obtain the p_T of the track. A track candidate is required a 3-out-of-4 coincidence for two gas gaps in each of TGC2 and TGC3 both in R and ϕ. This gives a low-p_T coincidence. The track is said to be high-p_T coincidence if a 2-out-of-3 coincidence for wires and a 1-out-of-2 coincidence for strips are found in TGC1. In the final stage of the trigger algorithm, two-dimensional patterns
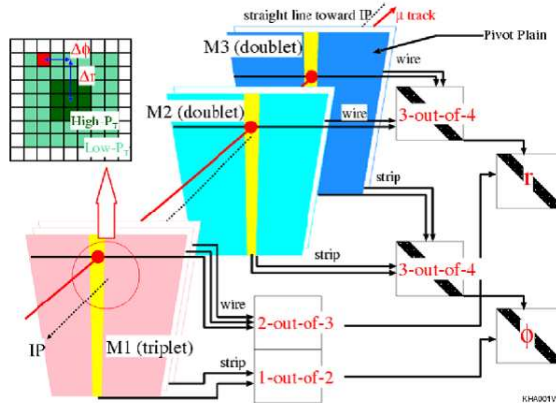

Figure 4.9: A schematic drawing of the coincidences and p_T determination of the L1 TGC trigger system.

of the deviations in both R and ϕ are used to determine the p_T of the track. EI/FI are reserved for future use.

4.3   L2 muon trigger

The aim of the L2 muon trigger is to improve measurements of p_T of muons and rejecting background from tracks found in the L1 muon trigger. At the L2 trigger, full detector information inside an RoI can be used for analysis. The L2 muon trigger consists of a number of selection algorithms. These algorithms can be grouped according to their purposes. An algorithm for the muon stand-alone tracking, TrigmuFast (μFast), finds trajectories of muons by using hits only in the RoI of the muon system to calculate the p_T. TrigmuComb combines the trajectories found in TrigmuFast and L2ID tracks reconstructed by the inner detectors. Other algorithms, for example TrigDiMuon and TrigmuIso, are more physics oriented algorithm to tag specific types of muons like dimuon events or isolated muons.

4.4   TrigmuFast

TrigmuFast is the reconstruction algorithm which is performed at the first stage of L2 muon trigger. The aim is to measure p_T more precisely than in the L1 muon trigger by using hit

information in the MDT chambers. The result of TrigmuFast is also used as a seed of other selection algorithms. The detail of TrigmuFast is described in the next chapter.

4.5   TrigmuComb

TrigmuComb matches trajectories in the track collection, which contains ID tracks for inner detector and MS tracks for muon system reconstructed by TrigmuFast, in space, for improving the quality of reconstructions. For non-isolated muons, the track collection corresponding to an RoI may contain many ID tracks. The matching is performed in (η, ϕ) plane and the track properties of the best-matched combination are calculated as a weighted average of the result. This weight is based on the resolution of p_T. TrigmuComb also gives rejection power for the muon from decay-in-flight of π/K and the fake track by cavern background in muon system, since such background sources likely do not have matching ID tracks or matches with an ID with large impact parameter.
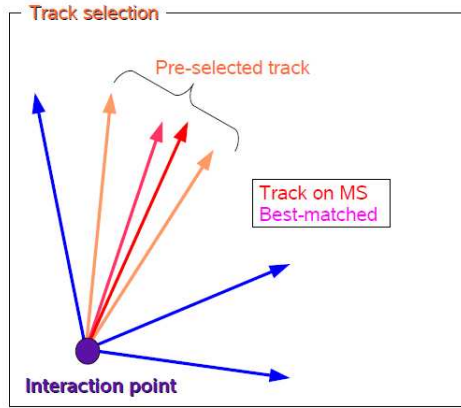

Figure 4.10: A track marked as the "best-matched" track is selected based on the χ^2.

Chapter 5

TrigmuFast

As described in chapter 4, the TrigmuFast is used in the first stage of the L2 muon trigger. This reconstruction algorithm measures p_T more precisely than the L1 muon trigger by making use of the information of the precise muon tracking detector, MDT. The events are selected based on this precisely measured p_T. In this chapter, the algorithm and performance of the TrigmuFast are described.

5.1 Algorithm

The algorithm consists of 3 major steps; "Pattern Recognition", "Track Fitting" and "p_T Estimation". The detail of each step is explained in the following sub-sections.

5.1.1 Pattern Recognition

The goal of the Pattern Recognition is to select MDT tubes relevant to the muon identified by the L1 muon trigger. At most one MDT tube per each layer is selected. This selection is done based on the muon trajectory defined by the L1 muon trigger, as schematically depicted in Fig. 5.1. Two red thick lines in the figure represent the RPC chambers, and the green circles represent the MDT tubes which make up a MDT chamber module. The hashed and filled circles show the MDT tubes in which hit information is recorded. The dashed line is the muon trajectory defined by the L1 trigger. A "road" is then defined with respect to the L1 muon trajectory, which is shown as two solid lines in the figure. All MDT tubes which have hit information and is located within the "road" are collected. If there are more than one MDT tubes in one layer, the one that has the least deviation from the trajectory is selected. This gives more robustness against fake hits due to, for example, thermal neutrons and photons filled in the experimental hall (called cavern background). These selected hits are then used in the next step, Track Fitting. In the end-cap region, the Pattern Recognition is processed in the same way.
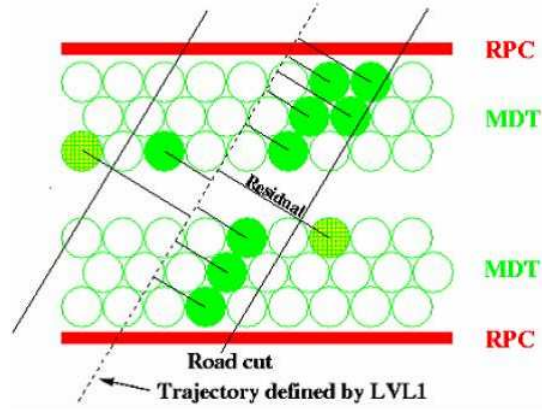
Figure 5.1: A schematic picture of Pattern Recognition

5.1.2 Track Fitting

In TrigmuFast, a trajectory in each MDT station is treated as a straight line. As described in Sect. 2, hit position measured by the MDT tube can be considered as a circle. Therefore, there is an ambiguity to determine the "left or right" side of the tube (left-right, L-R, ambiguity). An example is shown in Fig. 5.2.
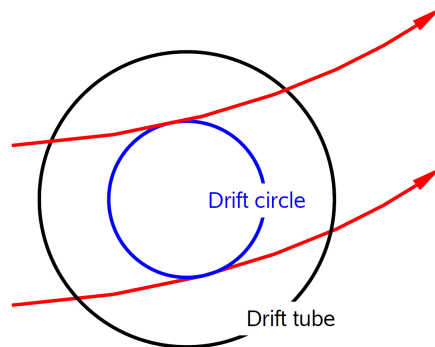

Figure 5.2: An illustration of the left-right ambiguity. A blue circle represents the drift circle. From one hit, two candidates of muon trajectory can be derived.

To solve this ambiguity and to define the muon trajectory, four hits among those selected in the Pattern Recognition are used. The reason of using only four but not all the MDT hits is to save the processing time. Two of the hits are picked up in the tubes nearest to the interaction points and the other two hits of the farthest. Then, all 16 combinations from the L-R ambiguity of the four tubes (i.e $2^4 = 16$) are examined in a χ^2 technique to find out the best combination, as follows. For each combination, a straight line is drawn according to the L-R assumption of the four tubes. Then, this assumption is examined whether other tubes are close enough to the straight line. The χ^2 is used for this evaluation, which is defined as a sum of "residuals" of all tubes:

41

$$\chi^2 = \sum_i^{tube} residual^2$$

The residual is defined as a distance from the straight line and the MDT hit position. Then, the best combination that gives the least χ^2 is chosen and hits with too large residuals are removed. Finally, the fitting result is used to define a pseudo-hit called super point, which represent both the position and direction of the fitted line at a middle of the each chamber layer.
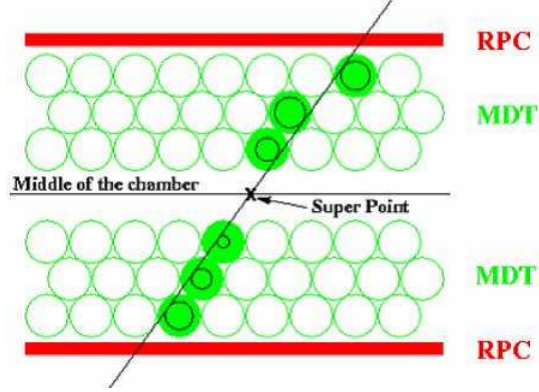

Figure 5.3: A schematic picture of Track Fitting

The Pattern Recognition and the Track Fitting are processed in every MDT station and three super points from inner, middle and outer stations are obtained.

5.1.3 Transverse momentum estimation (in the Barrel region)

A charged particle in an uniform magnetic field goes along a helix, and its trajectory in the plane perpendicular to the magnetic field is a circle. The relation between the momentum and the radius of this circle is given by the following equation,

$$p = 0.3 \times R \times B \tag{5.1}$$

where p is the mometum in unit of GeV, R is the radius of the circle in unit of meter, and B is the magnetic field in unit of Tesla. The toroidal magnetic filed in the barrel region is fairly uniform and thus trajectory of a charged particle can be regarded as a circle in the $R-z$ plane. The radius of the trajectory can be calculated by using more than two super points. In the TrigmuFast, a look-up table is used for the calculation of p_T in order to speed up the algorithm. The formula for the p_T calculation is given as follows;

$$p_T = A \times R + B \tag{5.2}$$

where the parameters A and B depend on hit position and thus are prepared for each small $\eta - \phi$ region. Their values in LUT are determined by using the Monte-Carlo simulation. In this p_T calculation, the energy loss of muon before entering the muon detector system, such as energy loss in calorimeters, are also corrected. That is, the p_T in the equation 5.2 can be considered as the muon momentum at the p-p interaction point.
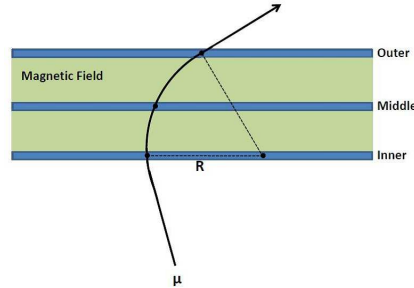

Figure 5.4: A schematic drawing on estimating p_T in barrel muon system

5.1.4 Transverse momentum estimation (in the Endcap region)

The p_T measurements in the endcap region is more complicated than in the barrel region. It is difficult to define a radius as in the barrel region, because the trajectory of a charged particle passed in the endcap region is generally not helix because of the non-uniformity of the magnetic field along the path of the particle. In TrigmuFast, two angles, α and β, which can be calculated by using the super points, are used for the p_T measurement. The definition of these angles are described below. The angle α is mainly used and supplemented by the β for the p_T calculation, because only the middle layer information is mandatory in the α determination and there is practically no area where α (and thus p_T) cannot be calculated. While, β gives generally better momentum resolution than α, but in some regions the β cannot be calculated because of lack of detector coverage in the inner station. In the following, details of the calculation for α and β are given.

- α

The angle α is calculated by using the position and direction information of the super point and the nominal interaction point. Figure 5.5 shows how α is calculated when the super point is found only in the middle station. In this case, α is defined as an angle between two lines; one is the direction of the superpoint, and the other is the line connecting the nominal interaction point and the position of the super point. The latter line corresponds to the trajectory of a muon, with an infinite momentum coming from the nominal interaction point. Figure 5.6 shows the case where super points are found both in the middle and outer layers. In this case, middle and outer super points are connected with a line, and the angle α is calculated as an angle between this line and the line connecting between nominal interaction point and the super point in the middle station.
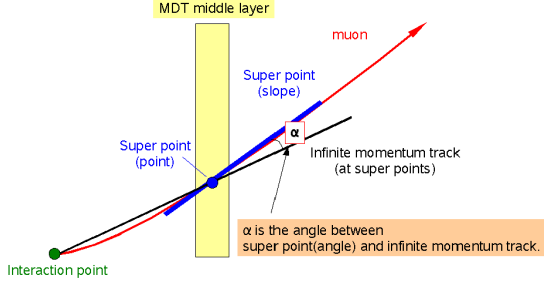
- β

Figure 5.5: A schematic view of the calculation of α when hits are found in only middle MDT station
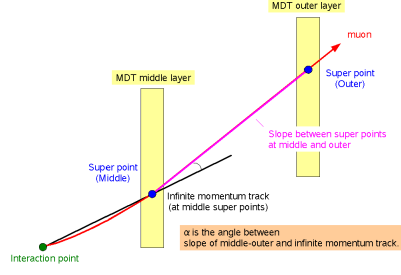

Figure 5.6: A schematic view of the calculation of α when the hits are found both in the middle and outer MDT station.

On the other hand, to calculate β, a super point must be found in the inner station. The angle β is defined in a similar manner as α; only the difference is using the direction defined by the super point in the inner station instead of the infinite momentum trajectory. By using this line, the β calculation is free from the assumption on the nominal interaction vertex. Figure 5.7 and 5.8 show how β is calculated in the cases where super points are found only in inner and middle layers, and in all layers, respectively.
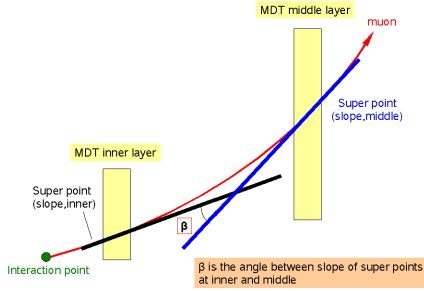

Figure 5.7: Calculation of angle β using the hits are found both in middle and outer MDT station.
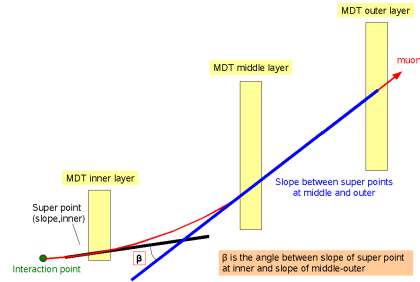
Figure 5.8: Calculation of angle β using the hits found in all the MDT station.

The relation between $\alpha(\beta)$ and p_T is given by the following formula.

$$\text{for } \alpha : \quad \frac{1}{p_T} = A_\alpha \times \alpha + B_\alpha$$
$$\text{for } \beta : \quad \frac{1}{p_T} = A_\beta \times \beta + B_\beta$$

In the formula, A and B are position dependent parameters. The Monte-Calro truth p_T is used for determing the parameters A and B. The p_T measurement is performed in a similar way to the Barrel region, namely by using LUTs.

5.2   Performance

The performance of the TrigmuFast is evaluated by using simulated single muon samples for different p_T values. The study was done separately in four η regions; $|\eta| < 1.0$, $1.0 < |\eta| < 1.5$,

$1.5 < |\eta| < 2.0$ and $2.0 < |\eta| < 2.4$, because the uniformity of the magnetic field is different in the regions.

5.2.1 p_T resolution

The resolution is given by the width of the distribution for the deviation of $\frac{1}{p_T}$, which is calculated by following formula,

$$ deviation\ of\ \frac{1}{p_T}\ :\ \frac{\frac{1}{p_T\ (TrigmuFast)} - \frac{1}{p_T\ (truth)}}{\frac{1}{p_T\ (truth)}} $$

where $p_T\ (TrigmuFast)$ means the measured p_T in TrigmuFast, and $p_T\ (truth)$ means the truth p_T at the interaction point in Monte-Carlo simulation. The plots for the p_T resolution are shown in Fig. 5.9. The plot in the left side is the resolution as a function of p_T truth, and the right side is the one as a function of $\eta - \phi$. The resolution in the barrel region is typically 2% at p_T (truth)
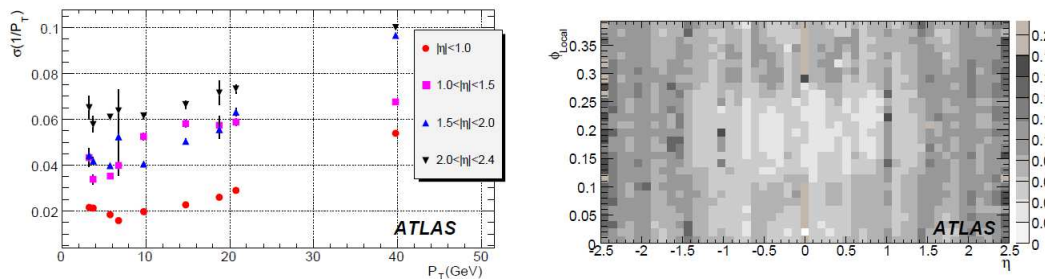

Figure 5.9: Resolution by TrigmuFast[16]

<10 GeV, and it increases as p_T truth gets higher, reaching to about 5% at p_T (truth)=30 GeV. In the endcap region, the resolution is generally worse than that in the barrel region, 5% at p_T (truth) <10 GeV, increasing up to 10% at p_T (truth)=40 GeV.

5.2.2 Trigger efficiency

Trigger efficiency is in general, the ratio of the numbers of the triggered and all generated events, where triggered means passing the trigger criteria. In the muon trigger, each trigger criterion is based on measured the p_T value. For example, the trigger "MU4" refers to the logic aiming for selecting muons with $p_T(truth) >4$GeV, which is realized as a practical cut of $p_T(measured) >3.2$GeV for instance for the barrel region. These thresholds on the measured p_T value are affected by the p_T resolutions discussed in the previous section. In this section, by using single muon Monte-Carlo events, we define the efficiency of the TrigmuFast as follows:

$$ \text{TrigmuFast efficiency}\ =\ \frac{\text{number of triggered muons passing L1 and TrigmuFast}}{\text{number of all generated muons}} $$

Note that this efficiency by definition includes also the L1 trigger efficiency, because TrigmuFast runs only on muon candidates which pass L1. Figure 5.10 is the trigger efficiency of TrigmuFast
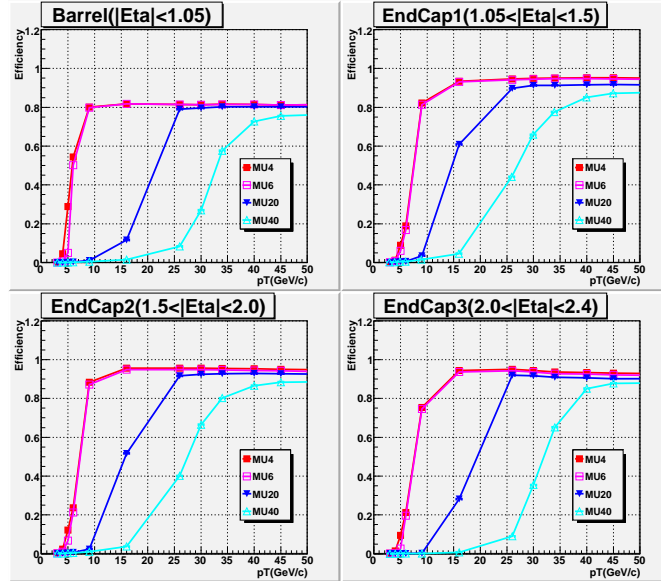
Figure 5.10: TrigmuFast efficiency, as defined in the text, shown as a function of p_T truth

as a function of $p_T(truth)$. It also shows the efficiency separatery for $|\eta| <$1.05, 1.05$< |\eta| <$1.5, 1.5$< |\eta| <$2.0 and 2.0$< |\eta| <$2.4. The efficiencies show a clear turn-on behavior; i.e, as the p_T gets higher it starts to turn on from zero around the threshold, reaching to a plateau with the efficiency typically 90% for all η regions and for all MU4, MU6, MU20, and MU40 triggers.

5.2.3 Trigger rate

The number of triggered events per second expected at a given instantaneous luminosity is called trigger rate. The muon trigger rate at the TrigmuFast (R) can be calculated from the muon production cross section ($d\sigma/dp_T$), the instantenous luminosity (L) and the trigger efficiency (ϵ) of TrigmuFast defined in the previous section, as follows:

$$R = L \int \frac{d\sigma}{dp_T}\epsilon(p_T)dp_T. \tag{5.3}$$

The muon production cross section at the LHC is shown in Fig. 5.11. In the region where muon p_T is less then a few GeV, the contribution from the π and K particles decay in flight dominates, and its cross section increases very rapidly as p_T gets lower. Although the trigger efficiency in such low p_T region is quite small, the large cross section may give substantial trigger rates. In addition, such low p_T muon production cross section from π and K particles is not only just large but also difficult to be precisely predicted. Thus, there are large uncertainties in the low p_T muon production, which in turn bring large uncertainty in the trigger rate estimation. The trigger rate at low p_T region may increase significantly with a slight increase of the trigger efficiency.
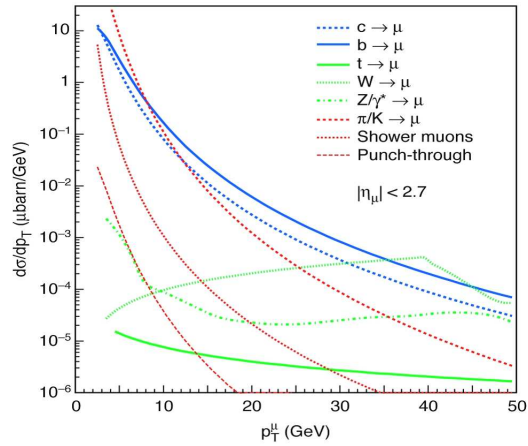
Figure 5.11: The cross section of muon at the LHC

L2 muon standalone trigger rates						
	$\mathscr{L} = 10^{31}\mathrm{cm}^{-2}\mathrm{s}^{-1}$		$\mathscr{L} = 10^{33}\mathrm{cm}^{-2}\mathrm{s}^{-1}$		$\mathscr{L} = 10^{34}\mathrm{cm}^{-2}\mathrm{s}^{-1}$	
	Barrel(Hz)	Endcap(Hz)	Barrel(Hz)	Endcap(Hz)	Barrel(Hz)	Endcap(Hz)
	4GeV		6GeV		20GeV	
π/K	190	140	4300	3700	410	1800
beauty	50	67	3000	3900	540	1500
charm	70	94	4000	5200	520	1700
top	<0.1	<0.1	<0.1	<0.1	0.2	0.4
W	<0.1	<0.1	3	4	24	38
TOTAL	310	301	11300	1280	1494	5038
	5GeV		8GeV		40GeV	
π/K	82	120	840	1500	200	690
beauty	37	59	1000	2200	87	280
charm	49	81	1300	2900	83	290
top	<0.1	<0.1	<0.1	<0.1	0.1	0.2
W	<0.1	<0.1	3	4	17	23
TOTAL	168	260	3143	6604	387	1283

Table 5.1: Rate at TrigmuFast [16].

Table 5.1 shows the single muon trigger rate with TrigmuFast for three different luminosity assumptions. For each case, two trigger thresholds are applied; 4GeV and 5GeV for the $L = 10^{31}\mathrm{cm}^{-2}\mathrm{s}^{-1}$, 6GeV and 8GeV for the $L = 10^{33}\mathrm{cm}^{-2}\mathrm{s}^{-1}$ and 20GeV and 40GeV for the $L = 10^{34}\mathrm{cm}^{-2}\mathrm{s}^{-1}$. The trigger rate in the endcap region is larger than that in the barrel region, because of the less rejection power for low p_T muons due to worse p_T resolution. To reduce the trigger rate from low p_T muons, improving the selection algorithm of TrigmuFast to such low p_T muons is needed.

5.3 Possible reason of the worse p_T resolution for low p_T muons in the endcap region

In the endcap muon system, the precise p_T measurement of muon is difficult when a muon passes through the region where the magnetic field is non-uniform. For example, in the region with weak magnetic field, the trajectory of low p_T muon gets similar to thet of high p_T muons. So these low p_T muons may be miss judged as high p_T muons if the direction of particle was mis-measured or bended by multiple scattering. The current TrigmuDast algorithm measures the p_T using the direction and position of the trajectory. When using α, it determines the bending angle after passing through the volume with the toroidal magnetic field. If the field has a complicated profile, the bending angle may not necessarily. Figure 5.12 shows such an example of the trajectory in the non-uniform magnetic field. In this case, the deviation of the direction of trajectory in the middle station is measured small although the bending radius is small and thus the change in the direction at each point is large. As a consequence the p_T of the trajectory is measured higher.
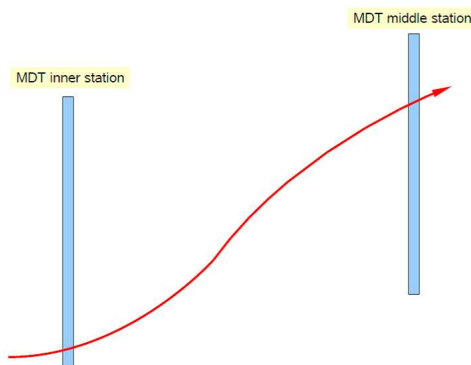

Figure 5.12: A example of the trajectory in complicated magnetic field

Three plots in Fig. 5.13 show the ratio of triggered muons in TrigmuFast with respect to muons, which passed the L1 muon trigger in the regions of $|\eta| < 1.0$, $1.0 < |\eta| < 1.5$, $1.5 < |\eta| < 2.0$ and $2.0 < |\eta| < 2.4$, respectively. The curves with circles represent the ratio of events passing
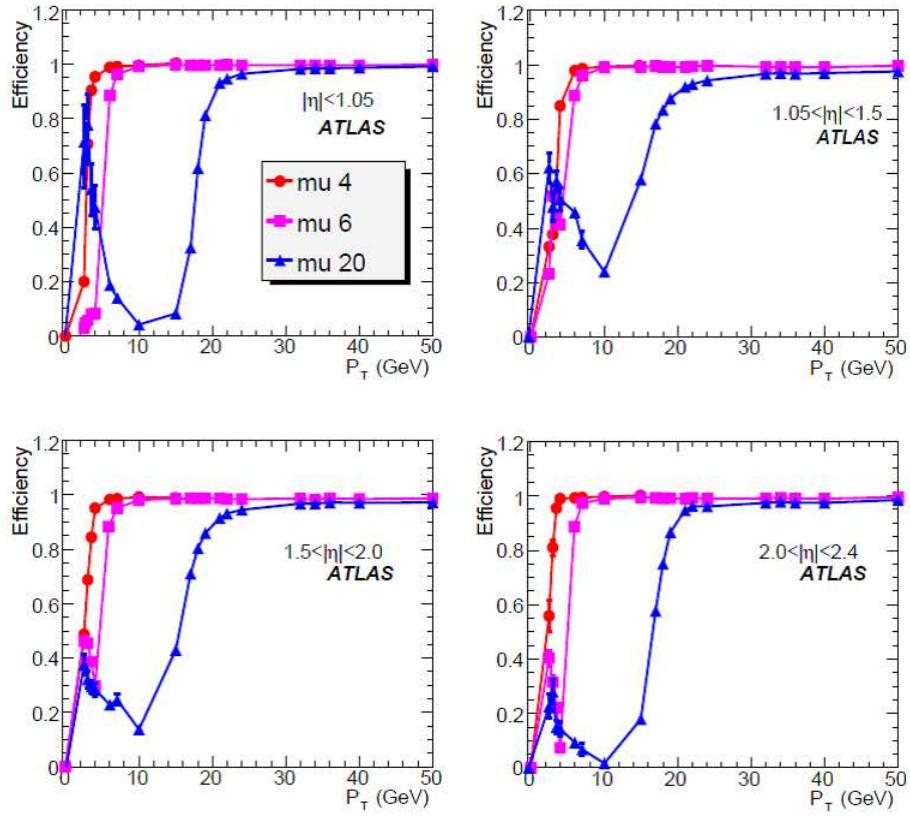
Figure 5.13: Trigger efficiency of the L2 TrigmuFast with respect to the events passing the L1 muon trigger, shown separately in four regions in η [16].

through the MU4 TrigmuFast trigger to that passing the L1 muon trigger. The plots with square and triangle represent the MU06 and MU20 threshold, respectively. Although muons with p_T less than a certain threshold should be rejected, about half of such muons are accepted in TrigmuFast.
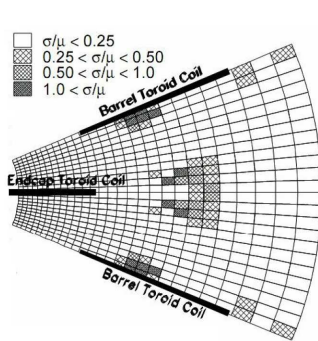

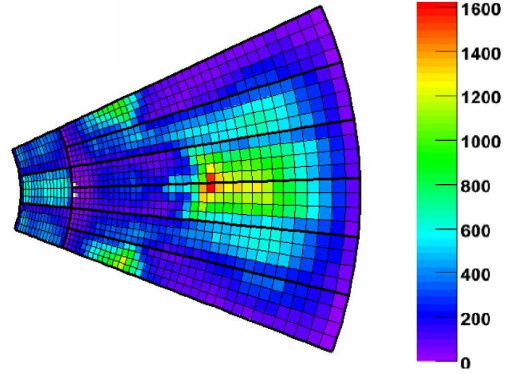Figure 5.14: The position of the regions in the end-cap system where momentum resolution is poor.

Figure 5.15: The hit map of the L1 muon trigger in the endcap region muons with p_T, measured by TrigmuFast less then 6GeV.

Chapter 6

The Kalman filter algorithm for tracking

As described in the chapter 5, TrigmuFast performs fast p_T measurement by using the LUTs. However, there remains some points to be improved for better performance, especially, the poor p_T resolution in the weak magnetic field regions. In order to overcome that, a new tracking method has been introduced by using Kalman Filter. Hereafter, this new method is called "muFastKalman", named after the algorithm used in the program.

6.1 Kalman Filter

Exactly speaking, a trajectory of a charged particle passing through the magnetic fields is distorted from helix because the curvature varies due to the energy loss in detectors. In addition, trajectory may have kinks by the effect of multiple scattering, as shown in Figure 6.1. Thus, it is difficult to describe such a trajectory by a simple formula with small number of parameters and fitting with the least-squares method is not suitable to reconstruct the track. It is known, however, that the Kalman Filter algorithm works well for such a case. In general, a track is described by a set of parameters, each of which defines the position and the direction of momentum at a measurement point. In Kalman Filter, these parameters are re-calculated and corrected by using measured value at every point along the trajectory. Thus, effects of multiple scattering and energy loss are taken into account.
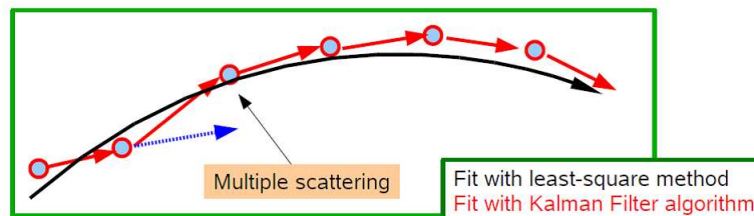

Figure 6.1: A conceptual drawing for the Kalman Filter algorithm

6.1.1 Algorithm

In this section, the basic idea of Kalman Filter is explained by taking an example of a simple phenomenon. Suppose that a charged particle travels in a plane perpendicular to an uniform magnetic field. Here, it is assumed that the position and direction of the track are measured at n-points as shown in Figure. 6.2. The trajectory of the particle will be a perfect circle without energy losses or multiple scattering. In reality, however, the trajectory may deviate from the circle and measurements have errors. The parameters to define the track at a measurement point are; x, and y are position informations, θ is direction information and Q/p is the charge over the momentum of the particle. The suffix "m" represents "measured" values and "e" presents "estimated" values. Parameters without "m" or "e" mean the optimized parameters as results of the Kalman Filter at each measurement point. "1" to "n" means the order of the measurement points along the trajectory.
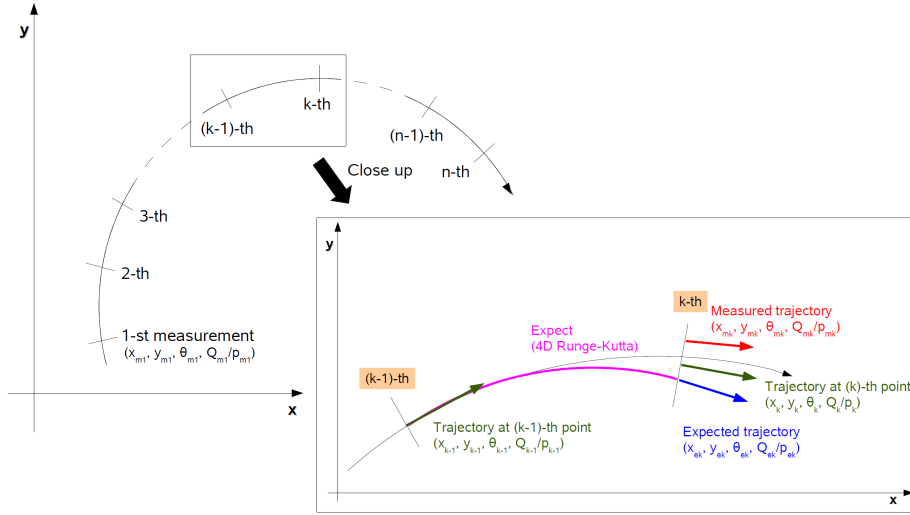

Figure 6.2: An example of Kalman Filter algorithm

The Kalman Filter algorithm consists of three phases, "prediction", "filtering" and "smoothing". In the "prediction" phase, the track is extrapolated by using optimized parameters at (k-1)th point and parameters at the k-th point are estimated. At the "filtering" phase, parameters are optimized by comparing estimated parameters and measured values at the k-th point. After "prediction" and "filtering" are performed at all measurement points along the trajectory, "smoothing" is processed. The aim of "smoothing" is to correct the optimized parameters at all measurement point in the Kalman Filter. For example, parameters at k-th point are optimized by using the "past" measured values from 1 to k. That is to say, these parameters does not include the measurement values in "future" from k+1 to n. To obtain the optimized parameters with all measurement values, the reverse ordered filtering from n to 1 is performed in the smoothing phase.

As described, Kalman Filter estimates and fits the parameters at every measurement point.

Therefore, the trajectory is reconstructed correctly by taking into account the multiple scattering and energy loss.
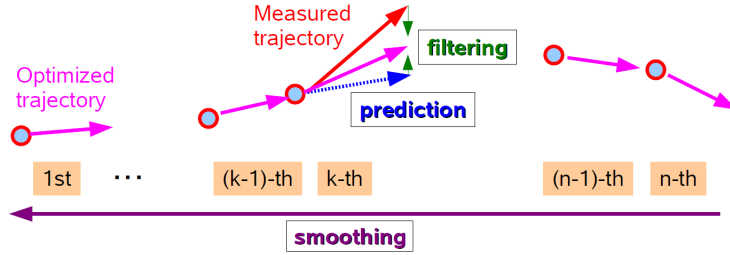

Figure 6.3: A schematic view of "prediction", "filtering" and "smoothing" in a fitting.

6.2 Coordinates and parameterization for muFastKalman

In this section, "Track State" and "Filtering Node" used for the Tracking in muFastKalman are described together with the coordinate system. Track State is a set of parameters which defines the track, and the information at measurement points are called as Filterng Node as shown in Fig. 6.4
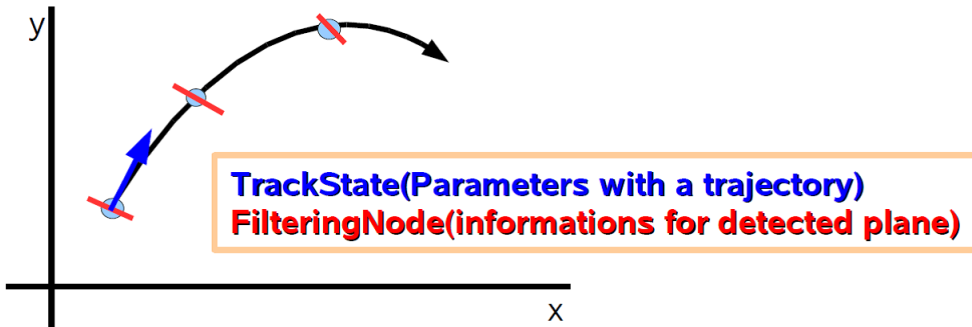
Figure 6.4: Filtering Node and Track State

6.2.1 The coordinate system

Two types of coordinate systems are used in muFastKalman. One is the global coordinate system common in the ATLAS experiment as described in chapter 3. The other one is the local coordinate system defined in each layer of tubes in the MDT. Figure. 6.5 shows local and global coordinate system in the endcap muon system. The local coordinate system is defined for every hit tube in MDT chamber. The origin of x and y in the local system is the center of on MDT tube. The relations for the axis are in local and global are; the R-axis in global coordinate system corresponds to the x-axis in local and the z-axis is common in local and global. The origin of z axis is shifted to the intersection of a track and a drift circle of MDT. The rotation matrix from the global to the local coordinate system is given by Eq. 6.1, where ϕ is the angle between x-axis

in global and x-axis in local. In the endcap muon system, positions are measured in local-x and local-z coordinates by the MDT tubes. The measured value for position in local-x is calculated from drift length measured in the MDT, and local-z is given by the location of MDT chamber.

$$\begin{pmatrix} \cos\phi & -\sin\phi & 0 \\ \sin\phi & \cos\phi & 0 \\ 0 & 0 & 1 \end{pmatrix} \tag{6.1}$$

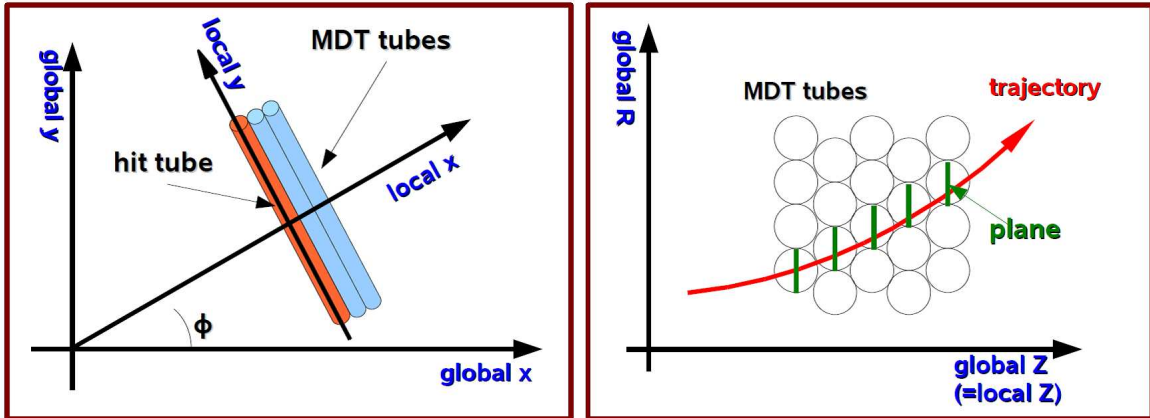Figure 6.5: Local coordinate system in the x-y and R-z view of global coordinate system. z-axis is common in local and global coordinate system.

6.2.2 Filtering Node

Filtering Node is a set of parameters concerning a measurement point. It includes two kinds of information. At first, parameters to define the measurement plane are included. These parameters are center position and a normal vector of the plane and a rotation matrix from local to global coordinate system. In the endcap region, the measurement plane is perpendicular to the beam axis (i.e. z-axis) and located at the intersection point on the z-axis between the drift circle and the pre-determined track, where the pre-determined track is the reconstructed track from the super point defined in the TrigmuFast as described in section 5.1.2. Thus a measurement plane is defined for each tube in the MDT with a hit at the center position and the normal vector in the local coordinate system. Rotation matrices are prepared for convenience. Secondly, Filtering Node contains the measurement position along the x-axis in local and its error. The MDT measures the drift length, and only local x-coordinate can be determined in the measurement plane.

No detectors are provided in regions between inner and middle, and middle and outer MDT chambers. These detector gaps are about 6 to 7 m, which are too long to extrapolate the track from a node to node. Therefore, some "virtual" Filtering Nodes (virtual node) are inserted and the track is extrapolated between these nodes as shown in Fig. 6.6. Virtual nodes are placed

every 100 mm across the gaps. They have a same set of parameters as the Filtering Node, but there are no measurement on the position and its error. Therefore, the measurement values at all virtual nodes are set to zero, and no "filtering", i.e. updating the parameters, is performed at these nodes.
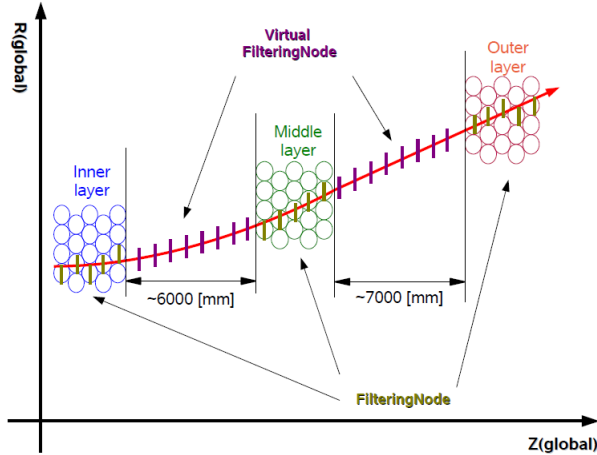

Figure 6.6: A schematic view of Filtering Nodes in the endcap muon system. Measurement planes at Filtering Nodes are shown as green lines and ones at virtual nodes are shown as purple lines.

6.2.3 Track State

The Track State is a set of parameters to define the trajectory at each Filtering Node. It includes five parameters; local-x, local-y, ϕ, θ and Q/p. Errors of these parameters are also included. Local-x and local-y are position information on the measurement plane. The momentum direction of the particle is described by using the polar angle θ and the azimuthal angle ϕ in the global coordinate system. Q/p gives the momentum information.

The Track State at the first Filtering Node in processing the muFastKalman is given by values obtained by TrigmuFast. The value of local-x is calculated from the drift circle measured at first node, and θ is calculated from the super point defined in the Track Fitting in TrigmuFast described in 5.1.2. For the local-y, the position information from the TGC is used. The azimuthal angle ϕ is calculated from the hit information of the TGC technically provided by TrigmuFast. The momentum component of Q/p is given by the p_T calculated in TrigmuFast using α and β.

Errors for each parameter, which is the component of Track State, are given by a 5 by 5 covariance matrix. The diagonal components are the squared errors for five parameters and other components are the correlated errors of five parameters. The covariance matrix for the errors of

parameters are described as

$$
\begin{pmatrix}
\sigma_{xx}^2 & \sigma_{yx}^2 & \sigma_{\phi x}^2 & \sigma_{\theta x}^2 & \sigma_{\frac{Q}{p}x}^2 \\
\sigma_{xy}^2 & \sigma_{yy}^2 & \sigma_{\phi y}^2 & \sigma_{\theta y}^2 & \sigma_{\frac{Q}{p}y}^2 \\
\sigma_{x\phi}^2 & \sigma_{y\phi}^2 & \sigma_{\phi\phi}^2 & \sigma_{\theta\phi}^2 & \sigma_{\frac{Q}{p}\phi}^2 \\
\sigma_{x\theta}^2 & \sigma_{y\theta}^2 & \sigma_{\phi\theta}^2 & \sigma_{\theta\theta}^2 & \sigma_{\frac{Q}{p}\theta}^2 \\
\sigma_{x\frac{Q}{p}}^2 & \sigma_{y\frac{Q}{p}}^2 & \sigma_{\phi\frac{Q}{p}}^2 & \sigma_{\theta\frac{Q}{p}}^2 & \sigma_{\frac{Q}{p}\frac{Q}{p}}^2 ,
\end{pmatrix}
\tag{6.2}
$$

where σ is the error of parameter and suffix is the corresponding parameters.

The initial error values for local-x in the Track State are set as 0.01 mm^2 which is the typical value of the position resolution of MDT, and the same value is also given for local-y. As for ϕ and θ, these errors are derived from the position information and its resolution of MDT by using the error propagation method. Last one is the error of Q/p; the error of p is calculated from p_T resolution of the TrigmuFast. The non-diagonal components are initially set to 0, and updates in process of the Kalman Filter algorithm.
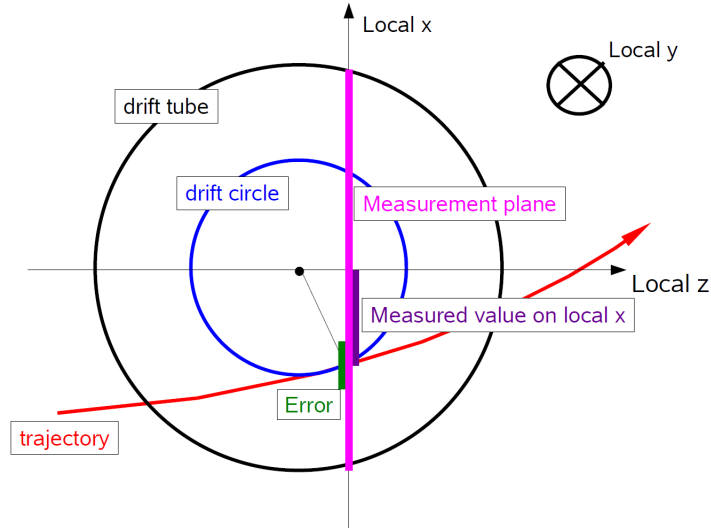
Figure 6.7: A view of measurement in a MDT tube on the local coordinate system. Two circles represent drift tube and drift circle. The trajectory is shown as the red line. The pink line is the measurement plane. The purple line and green line represent the measured position and its error along the x-axis in local.

6.3 Calculations in muFastKalman

6.3.1 Extrapolation of Track State in muFastKalman

In the "prediction" phase in muFastKalman, the Track State is extrapolated between the Filtering Nodes by taking into account the magnetic field. At the virtual nodes, the maximum

distance between Filtering Nodes is 100mm. At such region, extrapolating the Track State in one step degrades the precision in predicting the parameters. Therefore, the region between Filtering Nodes is divided into steps, which are very close to each other, and track is extrapolated between these steps. In the extrapolation, it is assumed uniform magnetic field and no energy loss in each step. The expected errors of the parameters included in the Track State at previous Filtering Node are used to update the Track State at the next Filtering Node taking into account the change of parameters the extrapolation.

6.3.2 Validation for measurement value

The measurement points are used in the "Filtering" process only if the point is close enough to the extrapolated Track State. For that, a value χ^2 is used, that is defined as

$$residual = (x_m - x_e) \tag{6.3}$$

$$\chi^2 = \frac{residual^2}{(\sigma_m^2 + \sigma_e^2)}, \tag{6.4}$$

where x_m is the measured value and x_e is the estimated value on local-x. The measurement point is used when the χ^2 values below the upper limit. With this procedure, the result of muFastKalman is not affected by obvious bad measurement.

6.3.3 Optimization of Track State

The estimated Track State is updated by using the measurement value of current Filtering node in the "filtering" phase. The calculation of "filtering" is based on two values: one is the residual which is defined Eq. 6.4, the other is the relevant errors of the parameters. The update value is calculated with following formula:

$$X_i = \frac{\sigma_{xi}^2}{(\sigma_{xm}^2 + \sigma_{xe}^2)} \times residual \ : \ i = x, y, \phi, \theta, \frac{Q}{p}, \tag{6.5}$$

where X is the updated value of the parameters responsible for its suffix and suffix i is the type of parameter. The obtained value X_i replaces to the parameters of estimated Track State. The error of parameters are calculated the following formula:

$$\sigma_{ij}^2 = \frac{\sigma_{ij}^2}{(\sigma_{xm}^2 + \sigma_{xe}^2)} \times \sigma_{ij}^2 \ : \ i, j = x, y, \phi, \theta, \frac{Q}{p}. \tag{6.6}$$

6.3.4 fitting order and region of the muFastKalman

The muFastKalman performs the fitting with reverse of time order and requires the hits in the inner MDT station. In the endcap muon system, only the region between the inner and middle MDT stationd has magnetic fields, and the L1 trigger is performed in the middle station. Therefore, it is natural to regard the region from middle to inner station as the core region of muFastKalman. When hits in outer station is found, they are supplementary used to obtain more precise information in the middle MDT station. That is to say, the fitting from outer to middle

can be regard as that of to obtain the precise TrackState for performing the more precise fitting from the middle to inner MDT stations. With these reasons, the muFastKalman performs its fitting in reverse time order and requires the hits in inner station.

6.3.5 The result of fitting

Figure 6.8 shows an example of fitting at the inner MDT station by muFastKalman. The displayed event is the simulated muon of which p_T is 16GeV. Circles in the figure show the drift circle in hit tubes. Blue lines show "filtered" tracks at previous Filtering Node and they are only displayed in the region of which tail. Red lines show the track after "prediction" in muFastKalman, they are only displayed initial region of its tracks. It is found that the muFastKalman traces hit tubes correctly.
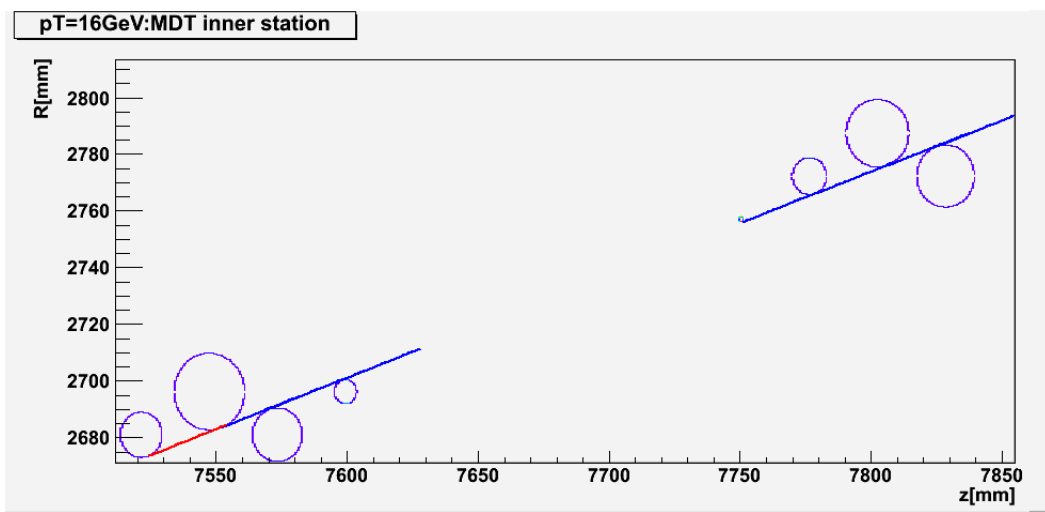

Figure 6.8: A view of the result of fitting by the muFastKalman in MDT inner station. The circles represent drift circles of hit tubes. Blue lines corresponds to the expected track in the fitting procedure, and red lines represent a track which performed "filtering" in the fitting procedure. The x-axis in this plot corresponds to z in global and y-axis matches R-axis.

Chapter 7

Performence of muFastKalman

7.1 Transverse momentum resolution

In the muon trigger, making the trigger decision is based on the measured p_T, therefore, the p_T resolution can be regarded as one of the parameter which represent the performance of the trigger algorithm. In this section, the p_T resolution obtained by using the muFastKalman is described. In following studies, the simulated muon, of which p_T is 16 GeV, events are used.

Figure 7.1 shows the distribution of p_T multiplied by charge, $p_T \cdot Q$, which is measured by the two selection methods, one is the muFastKalman shown with red line, and the other is the TrigmuFast which uses LUTs shown with black line. Comparing the two histograms, the center value of distribution obtained by muFastKalman is less than truth $p_T \cdot Q$. The reason of this shift is the effect of the energy loss in the calorimeters. In the reconstruction using muFastKalman, $p_T \cdot Q$ is measured at the entry point of the muon system, but in the reconstruction with TrigmuFast, $p_T \cdot Q$ at the nominal interaction point is used for LUTs. Between these two points, electromagnetic and hadron calorimeters are located and particles lose their energy by interaction with materials.
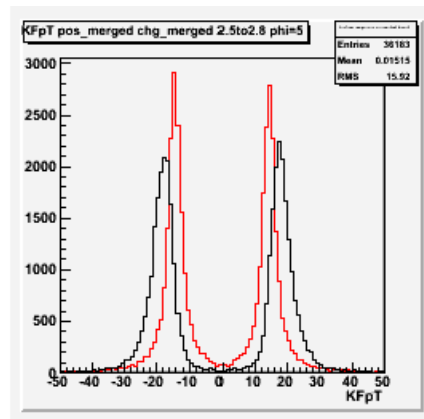

Figure 7.1: $p_T \cdot Q$ distribution obtained by each selection method using simulated single muon event with pT=16 GeV.

By using the measured p_T and Monte Carlo truth p_T, the deviation of p_T can be calculated, ant it is described as follows,

$$\text{deviation of } p_T = \frac{(1/\text{measured pT}) - (1/\text{Monte-Carlo truth pT})}{(1/\text{Monte-Carlo truth pT})} \tag{7.1}$$

As described above, muFastKalman and TrigmuFast give the p_T of a muon at different positions. In the calculation of p_T deviation using Formula 7.1, the truth p_T at suitable position is used for each method, namely p_T at the nominal interaction for TrigmuFast, and p_T at the entry point of the muon detector for the muFastKalman. Figure 7.2 shows histograms of p_T deviations. The resolutions of p_T are the following; 15.8% with the TrigmuFast and 14.3 % with muFastKalman. To obtain p_T resolution, a Gaussian fitting is performed to each histogram. The fitting is performed iteratively, and the range of the fitting is within two σ from the center value of distribution. Comparing these values, the muFastKalman can slightly improve the resolution. However, the distribution for muFastKalman has longer tail than one for TrigmuFast.
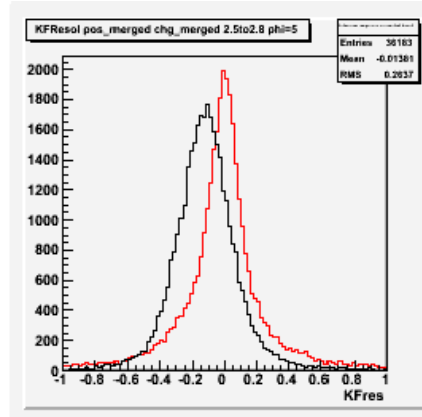

Figure 7.2: Histograms of the deviation of $p_T \cdot Q$. The x-axis is the deviation calculated in Formula 7.1.
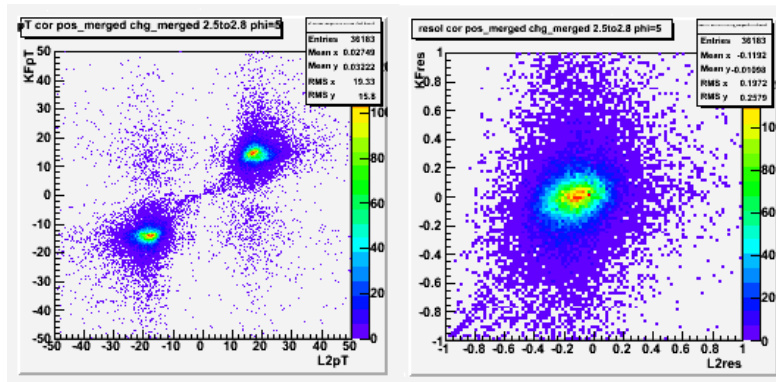

Figure 7.3: Correlation of p_T distribution and p_T resolution for TrigmuFast and muFasyKalman. In both plot, the x-axis is the result from TrigmuFast, and y-axis is muFastKalman. By using the muFastKalman, the tail events are increased, but the core resolution is improved.

7.1.1   position dependence

In the endcap muon system, two toroidal magnetic fields exist, one is generated by the barrel toroid magnet and the other is generated by the endcap toroid magnet. In the endcap region, most of particles pass through these two magnetic field geometrically, and integrated magnetic field along the trajectory has position dependence. Therefore, the performance of reconstruction also has position dependence.

To show these effect of the position dependence, the region of endcap muon system is divided into some regions and the resolution are calculated in every segmented region. The magnetic field has an octant symmetry along ϕ because eight magnet coils are located. Taking into account the symmetry of magnetic field, endcap muon system is divided into eight regions. This divided region is called "octant" as every octant has a similar magnetic field, all of them are aggregated into one octant. One octant is further divided into 25 regions in total, namely five regions along η and ϕ directions, respectively. Figure 7.4 shows the typical three histograms of p_T deviation
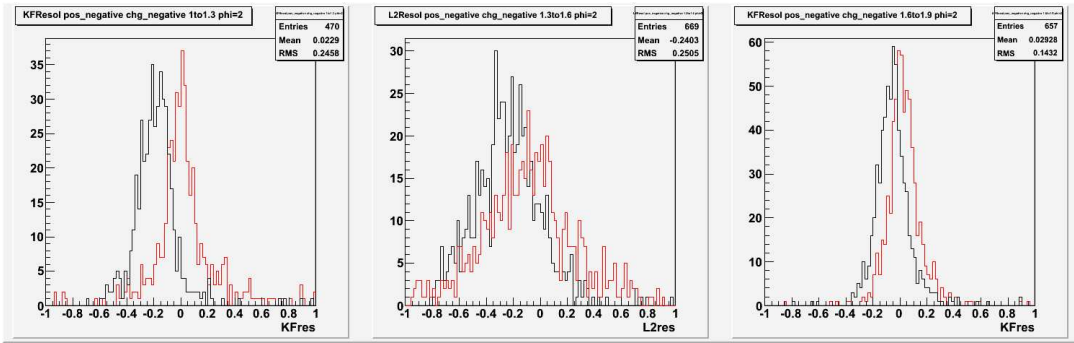

Figure 7.4: The p_T deviation measured by muFastKalman and TrigmuFast. Black line shows the result from TrigmuFast, and the red line is the result with muFastKalman. The region of η for each histograms are the left side is $1.0 < \eta < 1.3$, the center is $1.3 < \eta < 1.6$ and the right side is $1.6 < \eta < 1.9$. The region of ϕ is common to all histograms, $-\frac{\pi}{40} < \phi < \frac{\pi}{40}$.

picked up from 25 regions in an octant. From these plots, the center value of these plots with muFastKalman are close to 0 than TrigmuFast, which means that muFastKalman can recover more precise p_T for most of trajectories. The width of the resolution in high η region are smaller than TrigmuFast, but in low η region especially $1.3 \sim 1.6$ become larger. This low η region corresponds to the region where the integrated magnetic field is weak. On the other hands, high η region has uniform integrated magnetic fields. The p_T resolutions are affected by the intensity of the integrated magnetic field. One of the reasons of this result is the initial value of the muFastKalman. The initial value of the muFastKalman is used the result of TrigmuFast, and this result in these regions are already too worse. In addition, the integrated magnetic field in this region is too weak to recover the precise momentum in the muFastKalman. This is assumed as one of possible reasons that degrade the performance in such a region.

Chapter 8

Summary

Following the low luminosity run ($\mathscr{L} = 10^{33}$cm^{-2}s^{-1}), the LHC will be operated with the high luminosity ($\mathscr{L} = 10^{34}$cm^{-2}s^{-1}). With such high luminosity, production of huge number of low p_T muons are expected. Under such situations, the p_T resolution of the trigger algorithm is an important key to keep the muon trigger rate under its allowed limit.

The TrigmuFast at the second level of the ATLAS muon trigger performs a p_T measurement for muon candidates accepted in the L1 trigger. It achieves the fast processing of p_T measurement, however, there are some points to be improved for better p_T resolution as described in Chapter 5.

The p_T measurement in TrigmuFast does not take into account all effects which occur along the path of a particle, for example, the multiple scattering or a drastic chane of the magnetic field. To take into account such effects for the p_T measurement, a new track fitting procedure with Kalman Filter is developed. In this new procedure, the track parameters, which describe the track of a particle, are calculated and updated at every measured point. Therefore, the reconstructed track by this new procedure includes, for example, the effect of multiple scattering.

By applying this new method with Kalman Filter, the bias of p_T calculation was reduced about to 1% from 12% obtained with the TrigmuFast. On the other hand, applying Kalman Filter increases the tail of the p_T deviations, but the p_T resolution is improved from 15.8 % to 14.3 % in the total region of endcap muon system. The mean processing time increases from 2.38 ms to 4.38 ms.

In this thesis, it is confirmed that the development of muFastKalman gives the improvement of performances of L2 muon trigger below the maximum processing time. The muFastKalman is expected to be used in the online trigger algorithm and gives the precise p_T measurement.

Bibliography

[1] S. Weinberg "A Model of Leptons" 1967
Phys. Rev. Lett. 19, 1264-1266

[2] Sheldon L. Glashow "Partial Symmetries of Weak Interactions" 1961
Nucl. Phys. 22 579-588

[3] A. Salam "Elementary Particle Theory" 1968
Almquist and Wiksell, Stockholm

[4] Peter W. Higgs "Broken Symmetries and the Masses of Gauge Bosons" 1964
Phys. Rev. Lett. 13, 508-509

[5] Peter W. Higgs "Broken Symmetries, Massless Particles and Gauge Fields" 1964
Phys. Lett. 12, 132-133

[6] Peter W. Higgs "Spontaneous Symmetry Breakdown without Massless Bosons" 1966
Phys. Rev. 145, 1156-1163

[7] M. Spira P.M.Zerwars "Electroweak Symmetry Breaking and Higgs Physics" 1997
hep-ph/9803257

[8] CERN Public home http://public.web.cern.ch/public

[9] The ATLAS Magnet System http://atlas-ma.web.cern.ch/atlas-ma/

[10] The ATLAS Collaboration "ATLAS DETECTOR AND PHYSICS PERFORMANCE Technical Design Report Vol.1 and Vol2" 1999
CERN. Geneva. LHC Experiments Committee

[11] The ATLAS Collaboration "ATLAS Level-1 Trigger Technical Design Report" 1998

[12] The ATLAS Collaboration "ATLAS High-Level Trigger,Data Acquisition and Controls Technical Design Report" 2003

[13] The ATLAS Collaboration "The Calorimeter performance Techinical Design Report" 1997

[14] The ATLAS Collaboration "Muon Spectrometer Technical Design Report" 1997

[15] The ATLAS Collaboration "The ATLAS Experiment at the CERN Large Hadron Collider" 2008
   JINST 3 S08003

[16] The ATLAS Collaboration "Expected Performance of the ATLAS Experiment - Detector, Trigger and Physics" 2009
   arXiv:0901.0512